

# Strongly lensed SNe Ia in the era of LSST: observing cadence for lens discoveries and time-delay measurements

S. Huber<sup>1,2</sup>, S. H. Suyu<sup>1,2,3</sup>, U. M. Noebauer<sup>1</sup>, V. Bonvin<sup>4</sup>, D. Rothchild<sup>5</sup>, J. H. H. Chan<sup>4</sup>, H. Awan<sup>6</sup>, F. Courbin<sup>4</sup>, M. Kromer<sup>7,8</sup>, P. Marshall<sup>9</sup>, M. Oguri<sup>10,11,12</sup>, and T. Ribeiro<sup>13</sup>, The LSST Dark Energy Science Collaboration

<sup>1</sup> Max-Planck-Institut für Astrophysik, Karl-Schwarzschild Str. 1, 85741 Garching, Germany  
e-mail: shuber@MPA-Garching.MPG.DE

<sup>2</sup> Physik-Department, Technische Universität München, James-Frank-Straße 1, 85748 Garching, Germany

<sup>3</sup> Institute of Astronomy and Astrophysics, Academia Sinica, 11F of ASMAB, No.1, Section 4, Roosevelt Road, Taipei 10617, Taiwan

<sup>4</sup> Institute of Physics, Laboratory of Astrophysics, Ecole Polytechnique Fédérale de Lausanne (EPFL), Observatoire de Sauverny, 1290 Versoix, Switzerland

<sup>5</sup> Department of Electrical Engineering and Computer Science, University of California, 253 Cory Hall, Berkeley, CA 94720-1770, USA

<sup>6</sup> Department of Physics and Astronomy, Rutgers University, Piscataway, NJ 08854, USA

<sup>7</sup> Zentrum für Astronomie der Universität Heidelberg, Institut für Theoretische Astrophysik, Philosophenweg 12, 69120, Heidelberg, Germany

<sup>8</sup> Heidelberger Institut für Theoretische Studien, Schloss-Wolfsbrunnengasse 35, 69118 Heidelberg, Germany

<sup>9</sup> Kavli Institute for Particle Astrophysics and Cosmology, P.O. Box 20450, MS29, Stanford, CA 94309, USA

<sup>10</sup> Research Center for the Early Universe, University of Tokyo, 7-3-1 Hongo, Bunkyo-ku, Tokyo 113-0033, Japan

<sup>11</sup> Department of Physics, University of Tokyo, Tokyo 113-0033, Japan

<sup>12</sup> Kavli Institute for the Physics and Mathematics of the Universe (Kavli IPMU, WPI), The University of Tokyo, Chiba 277-8582, Japan

<sup>13</sup> LSST, 933 N. Cherry Ave., Tucson, AZ 85721, USA

Preprint online version: December 15, 2024

## ABSTRACT

The upcoming Large Synoptic Survey Telescope (LSST) will detect many strongly lensed Type Ia supernovae (LSNe Ia) for time-delay cosmography. This will provide an independent and direct way for measuring the Hubble constant  $H_0$ , which is necessary to address the current  $3.6\sigma$  tension in  $H_0$  between the local distance ladder and the early universe measurements. We present a detailed analysis of different observing strategies (also referred to as cadence strategy) for the LSST, and quantify their impact on time-delay measurement between multiple images of LSNe Ia. For this, we simulate observations by using mock LSNe Ia from the Oguri & Marshall lens catalog for which we produce mock-LSST light curves accounting for microlensing. To measure the time delay from the simulated observations we use the free-knot splines estimator from the software PyCS. We find that using only LSST data for time-delay cosmography is not ideal. Instead, we advocate using LSST as a discovery machine for LSNe Ia, enabling time delay measurements from follow-up observations from other instruments in order to increase the number of systems by a factor of 2 to 16 depending on the observing strategy. Further, we find that LSST observing strategies which provide a good sampling frequency (mean inter-night gap around 2 days) and high cumulative season length (10 seasons with season length around 170 days) are favored. Rolling cadences subdivide the survey and focus on different parts in different years; these observing strategies trade number of seasons for better sampling frequency, which leads in our investigation to half the number of systems in comparison to the best observing strategy. Therefore rolling cadences are disfavored because the gain from the increased sampling frequency cannot compensate for the shortened cumulative season length. We anticipate that the sample of lensed SNe Ia from our preferred LSST cadence strategies with rapid follow-up observations would yield an independent percent-level constraint on  $H_0$ .

**Key words.** gravitational lensing: strong - gravitational lensing: micro - supernovae: general - surveys - cosmological parameters - cosmology: observations

## 1. Introduction

The Hubble constant ( $H_0$ ) is one of the key parameters to describe the Universe. Current observations of the Cosmic Microwave Background (CMB), assuming a flat  $\Lambda$ CDM cosmology and the standard model of particle physics imply  $H_0 = (67.36 \pm 0.54) \text{ km s}^{-1} \text{ Mpc}^{-1}$  (Planck Collaboration 2018) which is in tension to  $H_0 = (73.52 \pm 1.62) \text{ km s}^{-1} \text{ Mpc}^{-1}$ , measured from the local distance ladder (Riess et al. 2016, 2018). In order to verify or refute this  $3.6\sigma$  tension, independent methods are needed.

One such method is lensing time-delay cosmography which can determine  $H_0$  in a single step. The basic idea is to measure the time delays between multiple images of a strongly lensed variable source (Refsdal 1964). This time delay, in combination with reconstructions of the lens mass distributions and line-of-sight mass structure, directly yields a “time-delay distance” which is inversely proportional to  $H_0$  (i.e.  $t \propto D_{\Delta t} \propto H_0^{-1}$ ). While the time-delay distance primarily constrains  $H_0$ , it also provides information on other cosmological parameters (e.g., Linder 2011; Jee et al. 2016; Shajib et al. 2018a;

Grillo et al. 2018). Applying this method to four lensed quasar systems, the H0LiCOW collaboration<sup>1</sup> (Suyu et al. 2017) together with the COSMOGRAIL collaboration<sup>2</sup> (Eigenbrod et al. 2005; Courbin et al. 2017; Bonvin et al. 2018) measured  $H_0 = 72.5^{+2.1}_{-2.3} \text{ km s}^{-1} \text{ Mpc}^{-1}$  in flat  $\Lambda$ CDM (Birrer et al. 2018), which is in agreement with the measurements using a local distance ladder but larger than CMB measurements.

Another promising approach goes back to the initial idea in Refsdal (1964) using lensed supernovae (LSNe) instead of quasars for time-delay cosmography. So far only two LSNe systems with resolved multiple images have been observed. The first one, called SN ‘‘Refsdal’’ discovered by Kelly et al. (2016a,b), was a 1987A-like Type II SN which was strongly lensed by the galaxy cluster MACS J1149.5+222.3. As shown in Grillo et al. (2018), with SN ‘‘Refsdal’’ one can measure  $H_0$  with a  $1\sigma$  statistical error of 7%. The second LSNe with resolved images is iPTF16geu reported by Goobar et al. (2017) from the intermediate Palomar Transient Factory (iPTF). The system is a SNe Ia at redshift 0.409 and strongly lensed by an intervening galaxy at a redshift of 0.216. Strong lens mass models of the system from More et al. (2017) yield SN image fluxes that are discrepant with the observations, which might be partly an effect of microlensing (Yahalomi et al. 2017; Foxley-Marrable et al. 2018). The models in More et al. (2017); Goobar et al. (2017) also predict very short time delays ( $\approx 0.5$  d) that can thus be significantly biased by microlensing time delay (Bonvin et al. 2018). Therefore it is important to include microlensing in LSNe studies.

Even though the number of LSNe is significantly lower than the number of lensed quasars, LSNe have some important advantages for measuring time delays. First, if they are observed before peak, the characteristic SN light curves make time-delay measurements easier and possible on shorter time scales in comparison to stochastically varying quasars. Second, supernova images fade away with time which facilitates measurements of lens stellar kinematics and therefore enables the combination of dynamics (Barnabè et al. 2011; Yıldırım et al. 2017; Shajib et al. 2018b) and lens mass modeling, to overcome degeneracies like the mass-sheet degeneracy (Falco et al. 1985; Schneider & Sluse 2014). Another way to overcome the mass-sheet degeneracy is the intrinsic luminosity of the source. Since SNe Ia are standardizable candles, LSNe Ia are very promising to break the model degeneracies in two independent ways.

Even though only two LSNe with resolved images are currently known, LSST will play a key role in detecting many more LSNe. We expect to find approximately 45 resolved LSNe Ia (Oguri & Marshall 2010) or 900 in total including unresolved ones (Goldstein & Nugent 2017, see also Quimby et al. 2014) over the 10 year survey. No other survey is capable of providing such high numbers. A remaining question, however, is how many of the detected systems will be valuable for measuring time delays and whether it will be possible to measure time delays just with the LSST data. The LSST cadence strategy (Marshall et al. 2017) is soon to be decided and the goal of this paper is to evaluate different cadences for our science case of measuring time delays in LSNe Ia. For this purpose, we investigate 20 different observing strategies. To simulate observations, we use mock LSNe Ia from the OM 10 catalog (Oguri & Marshall 2010), and produce the light curves for the mock SNe images based on synthetic observables calculated with ARTIS (Applied Radiative Transfer In Supernovae; Kromer & Sim

2009) for the spherically symmetric SN Ia model W7 (Nomoto et al. 1984). We employ magnifications maps from GERLUMPH (Vernardos et al. 2015) to include the effects of microlensing, similar to the approach followed by Goldstein et al. (2018b). We then simulate data points for the light curves, following the observational sequence from different cadences and uncertainties according to the LSST science book (LSST Science Collaboration 2009). To measure the time delay from the simulated observation, we use the free-knot splines estimator from PyCS (Python Curve Shifting; Tewes et al. 2013; Bonvin et al. 2016).

The structure of the paper is as follows. In Section 2 we present a theoretical calculation of microlensing on LSNe Ia. In Section 3 we introduce relevant information about LSST and different observing strategies investigated in this work. In Section 4, mock light curves of LSNe Ia are simulated and the time-delay measurement to quantify different LSST observing strategies is described in Section 5. The results are presented in Section 6 before we conclude in Section 7. Throughout this paper, magnitudes are given in the AB system.

## 2. Microlensing on Type Ia Supernovae

In this section we describe the calculation of microlensed SNe Ia light curves combining magnifications maps and a theoretical SNe Ia model. The relevance of microlensing on LSNe Ia has been shown theoretically by Dobler & Keeton (e.g., 2006), Goldstein et al. (2018b) and Bonvin et al. (2018) and, as mentioned before, the first detected LSNe Ia shows discrepancies between models and observation which might be partly due to microlensing (More et al. 2017; Yahalomi et al. 2017; Foxley-Marrable et al. 2018). Therefore to simulate more realistic light curves of LSNe Ia we include microlensing in our studies. In Section 2.1 we describe the magnifications maps we use. Section 2.2 explains the radiative transfer code ARTIS used to calculate synthetic observables. In addition the projection of the 3D simulation output to 1D is discussed including the geometrical delay as described by Bonvin et al. (2018). In Section 2.3 we present a comprehensive derivation of microlensed light curves of SNe Ia. Although it is based on Goldstein et al. (2018b), there are a few key differences. In particular we get a different redshift dependence for the observed SN flux since we account for differences in luminosity and angular diameter distances for the LSNe. This is important for our analysis that uses mock LSN systems at different redshifts.

### 2.1. Magnification maps for microlensing

Microlensing is the effect of additional magnification or demagnification caused by stars, or other compact objects with comparable properties, of the lensing galaxy. To model the effect of microlensing on a SN Ia we use magnification maps based on GERLUMPH (Vernardos et al. 2015, J. H. H. Chan et al. in preparation). These maps are created using the inverse ray-shooting technique (e.g., Kayser et al. 1986; Wambsganss et al. 1992; Vernardos & Fluke 2013) and are pixellated maps containing magnification factors  $\mu$  at the source plane. The 3 main parameters for the maps are the convergence  $\kappa$ , the shear  $\gamma$  and the smooth matter component  $s$  which is defined as the ratio of the smooth matter convergence  $\kappa_s$  to the total convergence  $\kappa$ . For

<sup>1</sup> <http://h0licow.org>

<sup>2</sup> <http://cosmograil.org>

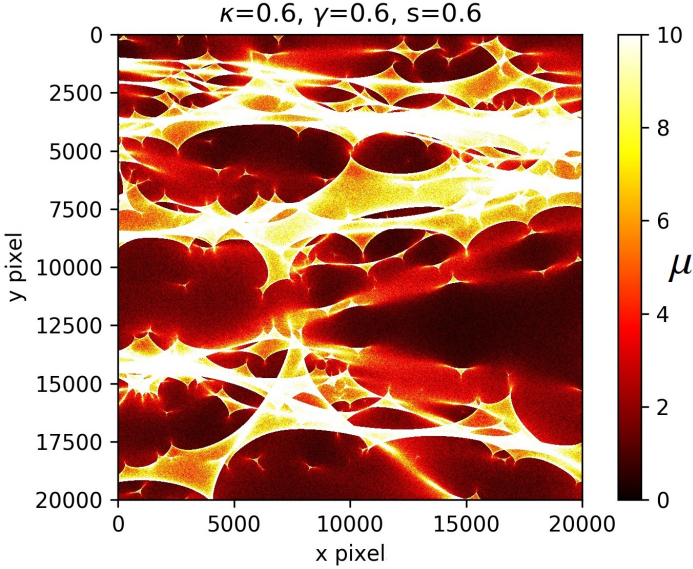


Fig. 1: Example magnification map for  $\kappa = 0.6$ ,  $\gamma = 0.6$  and  $s = 0.6$ . The color scheme illustrates the different magnification factors  $\mu$  at the source plane depending on the  $x$  and  $y$  coordinate. Many micro “caustics” are visible separating regions of high and low magnification.

simplicity, we assume  $s = 0.6$  in our investigation<sup>3</sup>. The Einstein radius  $R_{\text{Ein}}$  is the characteristic scale of the map, defined as

$$R_{\text{Ein}} = \sqrt{\frac{4G\langle M \rangle}{c^2} \frac{D_s D_{\text{ds}}}{D_d}}. \quad (1)$$

We assume a Salpeter initial mass function (IMF) with a mean mass of the point mass microlenses of  $\langle M \rangle = 0.35M_{\odot}$ . Details of the IMF are not relevant for our studies (J. H. H. Chan et al. in preparation).  $D_s$ ,  $D_d$  and  $D_{\text{ds}}$  are the angular diameter distances from us to the source, from us to the lens, and between the lens and the source, respectively. If we assume a flat  $\Lambda$ CDM cosmology and neglect the contribution of radiation, we can calculate the angular diameter distance via

$$D_A = \frac{c}{H_0(1+z_2)} \int_{z_1}^{z_2} \frac{dz}{\sqrt{\Omega_{m,0}(1+z)^3 + \Omega_{\Lambda,0}}}. \quad (2)$$

Our maps have a resolution of  $20000 \times 20000$  pixels and the total size of the maps is set to  $10R_{\text{Ein}} \times 10R_{\text{Ein}}$ . Therefore the size of one square pixel of the magnification map is

$$\Delta d_{\text{mag}} = \frac{10R_{\text{Ein}}}{20000} = \frac{1}{1000} \sqrt{\frac{G\langle M \rangle}{c^2} \frac{D_s D_{\text{ds}}}{D_d}}. \quad (3)$$

For the simulated LSST LSNe Ia in Section 4, the size of these microlensing maps ranges from  $4.12 \times 10^{-2}$  pc to  $2.70 \times 10^{-1}$  pc with a median of  $1.02 \times 10^{-1}$  pc. As an example, a magnification map for  $\kappa = 0.6$  and  $\gamma = 0.6$  is shown in Figure 1, where  $\Delta d_{\text{mag}} = 3.62 \times 10^{-6}$  pc.

<sup>3</sup> Goldstein et al. (2018b) investigated a few different  $s$  values and found that the effect of microlensing on LSNe Ia depends more on the spatial distribution of the radiation than on the precise  $s$  value. A further investigation of different  $s$  values will be presented in S. Huber et al. (in preparation).

## 2.2. Theoretical SNe Ia model and the 1D projection

To combine magnifications maps with SNe Ia, we adopt a similar approach as Goldstein et al. (2018b) where the spherically symmetric W7 model (Nomoto et al. 1984) and the Monte Carlo-based radiative transfer code SEDONA (Kasen et al. 2006) were used.

For our analysis, we also rely on the W7 model, but calculate synthetic observables with the radiative transfer code ARTIS (Kromer & Sim 2009), which stands for Applied Radiative Transfer In Supernovae and is a Monte Carlo based code to solve the frequency and time-dependent radiative transfer problem in 3D. Thus, ARTIS is not a deterministic solution technique, where the radiative transfer equation is discretized and solved numerically, but a probabilistic approach in which the radiative transfer process is simulated by a large number of Monte Carlo packets, whose propagation is tracked based on the methods developed by Lucy (1999, 2002, 2003, 2005). In this procedure,  $\gamma$ -ray photon packets from the radioactive decay of  $^{56}\text{Ni}$  to  $^{56}\text{Co}$  and the successive decay of  $^{56}\text{Co}$  to  $^{56}\text{Fe}$  are converted into UVOIR (ultraviolet-optical-infrared radiation) packets which are then treated with the full Monte Carlo radiative transport procedure. In the propagation of UVOIR packets, bound-free, free-free and especially bound-bound processes are taken into account. Once a packet escapes from the SN ejecta and the computational domain (which we refer to as a simulation box), the position  $\mathbf{x}$  where it escapes the simulation box, the time  $t_e$  when it leaves and the propagation direction  $\mathbf{n}$  are stored in addition to the energy and frequency. For the spherically symmetric ejecta the interaction of a photon packet stops after leaving the ejecta surface so in general before hitting the simulation box. For an illustration of 2 photon-packets leaving the simulation box in the same direction, see Figure 2.

To compare observations to theoretical models, one is typically interested in spectra and light curves. To get this information from numerical simulations, all escaping packets have to be binned in frequency and time, alongside the solid angle for asymmetric models. Since the microlensing effect depends on the location of the source as shown in Figure 1, spatial information of the SN is needed as well. Therefore, we have to project the 3D SN onto a 2D plane perpendicular to the observer and get the specific intensity as a function of wavelength, time and spatial coordinates  $x$  and  $y$ . Throughout this work, we assume that SNe Ia can be treated with spherical symmetry and therefore no binning in solid angle is necessary. While this is exact for an inherent 1D model like W7 and good for multi-dimensional simulations that lead to nearly spherically symmetric ejecta like some delayed detonations (Seitenzahl et al. 2013) and sub-Chandrasekhar detonations (Sim et al. 2010), this approximation is questionable for models that lead to strongly asymmetric ejecta like the violent merger (Pakmor et al. 2011, 2012).

In the 1D case, the spatial dependency of the specific intensity reduces to the dependency on the impact parameter  $p$ , i.e. the projected distance from the ejecta center. To construct this, we consider a plane containing the position  $\mathbf{x}$ , where a photon-packet has left the 3D simulation box, and the propagation direction  $\mathbf{n}$ . This is illustrated in Figure 2 for two packets leaving at different positions but propagating in the same direction. Because of the vast distance of the SN, the observer is defined as a plane perpendicular to  $\mathbf{n}$ . The radial coordinate where the photon leaves the box is  $r = \sqrt{x^2}$  and the angle between the position

vector  $\mathbf{x}$  and the propagation direction  $\mathbf{n}$  is  $\cos \theta = \frac{\mathbf{x} \cdot \mathbf{n}}{|\mathbf{x}| |\mathbf{n}|}$ . Then, the impact parameter is defined as

$$p = r \sin \theta = r \sqrt{1 - \cos^2 \theta}, \quad \theta \in [0, \pi]. \quad (4)$$

From Figure 2 we see that different photon-packets, leaving the box at different positions but at the same time after explosion  $t_e$ , will reach the observer at different times. If we assume that the orange packet from Figure 2 reaches the observer at time  $t'$  and the blue packet at time  $t$  we can relate both times via  $t = t' + \frac{d'-d}{c}$ , where  $d = r \cos \theta$  and  $d' = |\mathbf{x}'|$ . The time when the orange packet reaches the observer can be expressed as  $t' = t_e + C$ , where  $C$  is a constant defining the distance from the observer to the simulation box for the orange packet. From this we can write  $t = t_e + C + \frac{d'-d}{c}$ . Since the comparison to real observations is always performed relative to a maximum in a chosen band we are only interested in relative times. Therefore we can simplify the equation for  $t$  by defining a reference plane at the center of the SN perpendicular to the propagation direction  $\mathbf{n}$  (red dashed line). For this reference plane  $C = -\frac{d}{c}$  which leads to the observer time

$$t = t_e - \frac{r \cos \theta}{c}, \quad (5)$$

as defined in Lucy (2005) which accounts for the geometrical delay described in Bonvin et al. (2018). We will refer to the observer time  $t$  as the time since explosion. With the definition of the time  $t$  and the impact parameter  $p$ , the energy is binned in these two quantities<sup>4</sup> as well as in wavelength  $\lambda$ . The emitted specific intensity can then be calculated via

$$I_{\lambda,e} = \frac{dE}{4\pi dt d\lambda 2\pi p dp}, \quad (6)$$

where the factor  $4\pi$  is needed as a normalization over the unit sphere.

### 2.3. Microlensed flux of LSNe Ia

To calculate microlensed light curves we first have to determine the spectral flux for a SN, which can be calculated for a source of angular size  $\Omega_0$  on the sky as

$$F_\lambda = \int_{\Omega_0} I_{\lambda,o} \cos \theta_p d\Omega. \quad (7)$$

Here  $I_{\lambda,o}$  is the specific intensity at the position of the observer. In Figure 3 a spherical source (grey disc) is placed perpendicular to the line of sight at  $\theta_p = 0$ . The disc represents the projected emitted SN specific intensity  $I_{\lambda,e}$ . Since the source size is much smaller than the angular diameter distance to the source, we use the approximation for small angles and get  $\theta_p = \frac{p}{D_A}$  and  $\cos \theta_p \approx 1$ , which means that we assume parallel light rays. Therefore  $d\Omega = d\phi d\theta_p \theta_p = \frac{1}{D_A^2} d\phi dp p$  and the spectral flux can be expressed as

$$F_\lambda = \frac{1}{D_A^2} \int_0^{2\pi} d\phi \int_0^{p_s} dp p I_{\lambda,o}. \quad (8)$$

<sup>4</sup> Technical detail: Since the box is expanding with the SN over time the impact parameter  $p$  is a function of time. To eliminate this time dependency one can use the reasonable assumption that the SN is homologously expanding (Roepke 2005) and therefore simply divide the impact parameter by the observer time as in Goldstein et al. (2018b). The unit of this new impact parameter is therefore  $\text{cm s}^{-1}$  instead of cm and the unit of the new specific intensity is  $\text{erg s cm}^{-3}$  instead of  $\text{erg s}^{-1} \text{cm}^{-3}$ .

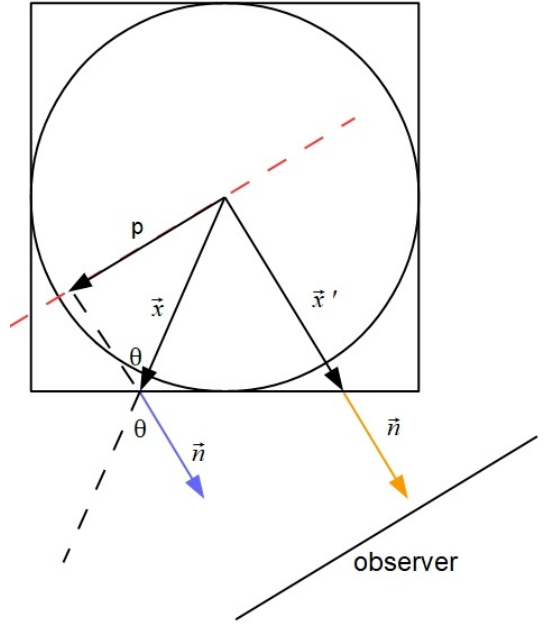


Fig. 2: Slice through a spherically symmetric SN enclosed in a 3D simulation box in order to explain the 1D projection of a SN. Two photon packets in orange and blue leave the box at different positions but propagating in the same direction. The observer can be illustrated as a plane perpendicular to the propagation direction of the photon packets because of its vast distance from the SN. Due to the tilt of the observer relative to the box, two packets leaving the box at the same time will reach the observer at different times. To take this into account an observer time  $t$  is defined which is measured with respect to the reference plane (red dashed line).

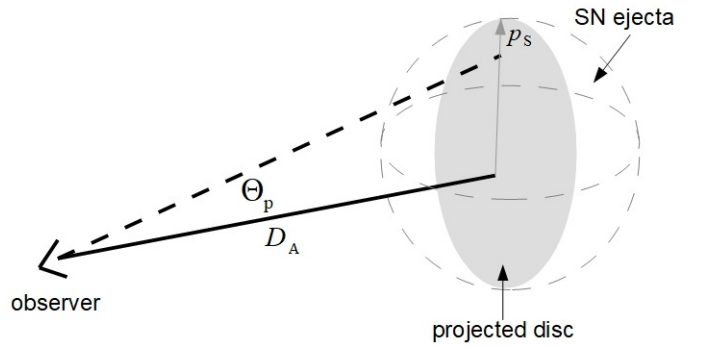


Fig. 3: A SN projected onto a disc perpendicular to the line of sight to the observer. The center of the disc with radius  $p_s$  is placed at  $\theta_p = 0$  at an angular diameter distance of  $D_A$  from the observer.

where  $p_s$  is the source radius of the projected disc. The next step is to relate the specific intensity at the observer's position to the source position. Hereby, we have to take into account that the specific intensity is redshift dependent. According to Liouville's theorem  $I_\nu/\nu^3$  is a conserved quantity in free space (Mihalas & Weibel-Mihalas 1999, page 414) and therefore we have  $I_\lambda \propto \lambda^{-5}$ . Since the emitted wavelength  $\lambda_e$  can be related to the observed

one,  $\lambda_o$ , via  $\lambda_o = \lambda_e(1+z)$  we find that  $I_{\lambda_o} = I_{\lambda_e}/(1+z)^5$ . Therefore by using  $D_L = (1+z)^2 D_A$  the spectral flux reduces to

$$F_\lambda = \frac{1}{D_L^2(1+z)} \int_0^{2\pi} d\phi \int_0^{p_s} dp p I_{\lambda_e}. \quad (9)$$

To add the effect of microlensing  $I_{\lambda_e}$  has to be replaced with  $\mu I_{\lambda_e}$ , which is possible since lensing conserves surface brightness. The value  $\mu$  is the microlensing magnification<sup>5</sup> as a function of  $\phi$  and  $p$ . Therefore we get

$$F_\lambda = \frac{1}{D_L^2(1+z)} \int_0^{2\pi} d\phi \int_0^{p_s} dp p \mu I_{\lambda_e}. \quad (10)$$

We note that this equation is slightly different from the one derived in Goldstein et al. (2018b), because we define the angle  $\theta_p$  via the angular diameter distance instead of luminosity distance. While this is not relevant for rest-frame spectra and light curves as discussed in Appendix A it is crucial for all other investigations in this work including redshift.

The projected specific intensity inferred from simulations is a discrete function in time, wavelength and impact parameter and denoted as  $I_{\lambda,e}(t_i, p_k)$ . Because of the spherical symmetry of W7, it has just a 1D radial dependency whereas the magnification map is obtained on a 2D cartesian grid. To combine both quantities as needed in Equation (10), it is necessary to transform one of both discrete quantities into the other coordinate system. We choose to interpolate the specific intensity onto a 2D cartesian grid:

$$I_{\lambda,e}(t_i, p_k) \rightarrow I_{\lambda,e}(t_i, x_l, y_m). \quad (11)$$

For this, we construct a cartesian grid with a pixel size  $\Delta x = \Delta y \equiv \Delta d_{\text{mag}}$ . To get accurate results,  $\Delta p \gtrsim \Delta d_{\text{mag}}$  is required but to save computational memory we restrict ourselves to

$$\Delta p \approx \Delta d_{\text{mag}}. \quad (12)$$

As the SNe Ia ejecta expand,  $\Delta p$  grows. Since  $\Delta d_{\text{mag}}$  is a fixed quantity defined by Equation (3), we interpolate the magnification map to a finer or coarser grid to fulfill the criteria in Equation (12) using the Python library `scipy`<sup>6</sup> (Jones et al. 2001). To get  $I_{\lambda,e}(t_i, x_l, y_m)$  for a given time  $t_i$  we interpolate  $I_{\lambda,e}(t_i, p_k)$  in  $p$  and evaluate it for all grid points  $(x_l, y_m)$ . Therefore the spectral flux at time  $t_i$  after explosion can be calculated via

$$F_{\lambda_j, \text{cart}}(t_i) = \frac{1}{D_L^2(1+z)} \sum_{l=0}^{N-1} \sum_{m=0}^{N-1} I_{\lambda_j,e}(t_i, x_l, y_m) \mu(x_l, y_m) \Delta d_{\text{mag}}^2. \quad (13)$$

For the calculation of fluxes and light curves for astronomical sources at redshift  $z$  we have to substitute

$$t \rightarrow (1+z)t \quad \text{and} \quad \lambda \rightarrow (1+z)\lambda. \quad (14)$$

To calculate microlensed light curves for the 6 LSST filters (details about LSST in Section 3) we combine Equation (13) with the transmission function  $S_X(\lambda)$  for LSST filter X. We calculate AB-magnitudes as described by Bessell & Murphy (2012) such that

$$m_{\text{AB},X}(t_i) = -2.5 \log_{10} \left( \frac{\sum_{j=0}^{N-1} S_X(\lambda_j) F_{\lambda_j, \text{cart}}(t_i) \Delta \lambda_j \lambda_j}{\sum_{j=0}^{N-1} S_X(\lambda_j) c \Delta \lambda_j / \lambda_j} \times \frac{\text{cm}^3}{\text{erg}\text{\AA}} \right) - 48.6. \quad (15)$$

<sup>5</sup> We break here with the traditional nomenclature adopted in radiative transfer, where  $\mu$  stands for  $\cos \theta$ . Instead,  $\mu$  denotes the magnification factor throughout this work.

<sup>6</sup> <https://www.scipy.org/>

for the magnitude at the  $i$ -th time bin for filter X.

Light curves in absolute magnitudes are shown in Figure 4 for the  $g$  and  $z$  bands. To measure time delays it is important to catch the light curve peaks of different images of a LSNe Ia. While we have a single peak for rest-frame light curves  $u$  and  $g$  we find a secondary peak in the redder bands where we could ideally catch both peaks for delay measurements. In addition to the non microlensed case (dotted black), light curves with microlensing (solid cyan and dashed violet) for two different positions (see left panel) in the magnification map from Figure 1 are shown. The microlensed light curves are highly distorted and peaks are shifted, which adds large uncertainty to the time-delay measurement between different images based on light curves that undergo different microlensing.

A more detailed investigation of microlensing is presented in Appendix A, where also spectra and color curves are discussed. We find from the investigated magnification map (Figure 1) an achromatic phase for some color curves up to  $\sim 25$  to 30 days, as reported in Goldstein et al. (2018b); however, other color curves show a shorter or non-existent achromatic phase. Our investigation also indicates that the achromatic phase depends highly on the specific intensity profiles and therefore the investigation of different explosion models is necessary to explore this further (S. Huber et al., in preparation). Furthermore, some color curves from ARTIS are different in shape from the ones of SEDONA, which is important to note since features like peaks are necessary to measure time delays. Even though color curves seem to be more promising for measuring time delays (as suggested by Goldstein et al. 2018b, and discussed in Appendix A), we use light curves instead for our further investigation because the sparse sampling of LSST does not provide directly color curves. Since color information is more easy to obtain with triggered follow-up observations, it is promising to develop color curve fitting methods in the future.

### 3. Large Synoptic Survey Telescope (LSST)

The LSST will target about  $20\,000 \text{ deg}^2$  of the southern hemisphere with a field of view of  $9.6 \text{ deg}^2$ . Observations will be taken in six broad photometric bands *ugrizy* and each position in the survey area will be repeatedly observed over time, where each ‘‘visit’’ is composed of 1 or 2 back-to-back exposures in the observing strategies currently under consideration. About 90% of the observing time will be spent on the  $18\,000 \text{ deg}^2$  wide-fast-deep survey (WFD), where the inter-night gap between visits in any filter is about 3 days (LSST Science Collaboration 2009). The rest of the time will be used for other regions like the Northern Ecliptic, the South Celestial pole, the Galactic Center and a few ‘‘deep drilling fields’’ (DDFs) where single fields ( $9.6 \text{ deg}^2$ ) will be observed to a greater depth in individual visits.

The scientific goals of LSST include exploring the nature of dark energy and dark matter, exploring the outer regions of the solar system and completing the inventory of small bodies in the solar system. These science goals restrict the cadence strategy but still leave a certain amount of freedom. For example, to detect fast-moving transients like asteroids, a revisit of an observed field within an hour is usually necessary. Such a revisit is planned if the first observation was taken in one of the bands  $g$ ,  $r$ ,  $i$  or  $z$  and is done in the same filter as the first observation for most of the cadence strategies under investigation in this work. For more details, see LSST Science Collaboration (2009).

As the LSST Project is in the process of finalizing the cadence strategy, this paper investigates how different cadence strategies will influence the possibility of measuring time delays

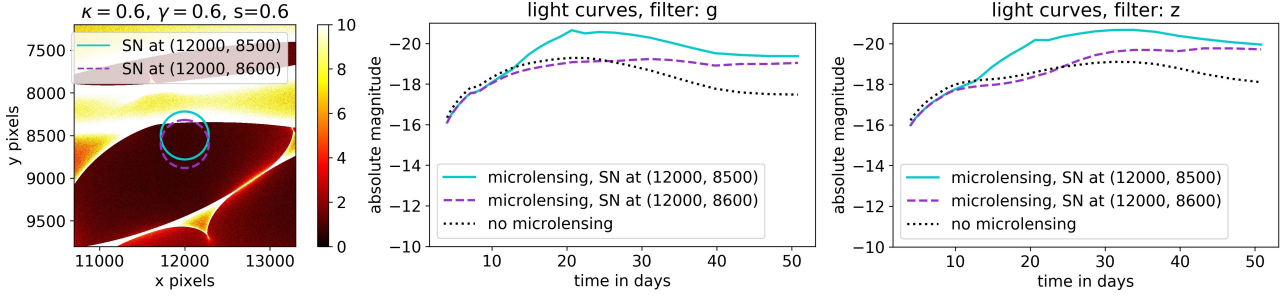


Fig. 4: Influence of microlensing on light curves  $g$  and  $z$  for two different positions (solid cyan and violet dashed) as shown in the left panel at 21 days after explosion for the magnification map of Figure 1. The case of no microlensing is shown as black dotted line in the middle and right panels. We see that microlensing can cause distortion of light curves, shift the peaks and therefore add uncertainties to time-delay measurements between images undergoing different microlensing.

for LSNe Ia. We specifically look at what is termed as a “rolling cadence”, where the overall idea is to subdivide the WFD and focus on different subdivided parts in different years, with the final 10-year static survey performance being the same as the nominal 10-year survey. This strategy is one way to provide a better sampling but it will reduce the number of seasons. A specific case for a rolling cadence is the one with two declination bands, which subdivides the WFD (with a declination from 0 to  $-60$  deg) into a northern region covering declination from 0 to  $-30$  deg and a southern one with declination in  $-30$  to  $-60$  deg. The idea is then to visit the northern part only in odd years (year 1, 3, 5, 7, 9) and the southern part in even years (year 2, 4, 6, 8, 10) or vice versa.

### 3.1. Observing strategies

We investigate 20 different observing strategies which are potential LSST cadences or of special interest for our science case. In Section 3.1.1 we present the different observing strategies. Readers who are more interested in the overall conclusions instead of specific details about the cadence strategies might directly jump to Section 3.1.2.

#### 3.1.1. Specifications of observing strategies

16 out of the 20 investigated cadence strategies are implemented with the OpSim scheduler<sup>7</sup> and the remaining 4 are produced by `alt_sched`<sup>8</sup> and the feature-based scheduler<sup>9</sup>. Both the OpSim and feature-based schedulers use a greedy algorithm, where the sky location of the next visit is determined by optimizing different parameters such as seeing, time lapsed since the last visit at the location, etc. In contrast, `alt_sched` employs a non-greedy algorithm by observing at minimum air mass and only relaxing on that to increase season length. The following key points describe the different observing strategies very briefly, where strategies with a capital letter have a larger than nominal  $18\,000\text{ deg}^2$  WFD footprint (the color scheme is explained in Section 3.1.2)<sup>10</sup>:

- `alt_sched`: Non-greedy algorithm; revisits in the same night in different filter; visits distributed in *ugrizy* as  $\sim (8.2, 11.0, 27.6, 18.1, 25.6, 9.5)\%$ .
- `alt_sched_rolling`: Same as `alt_sched` but as a rolling cadence with two declination bands.
- `baseline2018a`: Greedy algorithm like all following cadences; official baseline;  $2 \times 15$  s exposure; revisit within an hour in the same filter and scattered visits over WFD, 4 DDFs, Northern Ecliptic, South Celestial pole and Galactic Center; distribution of visits in WFD over *ugrizy* as  $\sim (6.8, 9.4, 21.5, 21.6, 20.2, 20.4)\%$ . For all following cadences up to `pontus_2506` just the main differences with respect to `baseline2018a` are listed.
- `colossus_2664`: WFD cadence over Galactic Plane.
- `colossus_2665`: Slightly expanded WFD.
- `colossus_2667`: Single visits instead of pair visits each night.
- `kraken_2026`: Unofficial baseline with improved slew time.
- `kraken_2035`: 9 DDFs instead of 4.
- `kraken_2036`: Standard WFD cadence in year 1, 2, 9 and 10 and a rolling cadence with three declination bands in between.
- `kraken_2042`: Single 30 s exposure instead of  $2 \times 15$  s exposure.
- `Kraken_2044`: Very large WFD footprint of  $24\,700\text{ deg}^2$ ; 5 DDFs; single visits instead of visits in pairs each night.
- `mothra_2045`: A rolling cadence in WFD (2 dec. bands).
- `Mothra_2049`: Similar to `mothra_2045` but on a very large WFD footprint ( $24\,700\text{ deg}^2$ ).
- `Nexus_2097`: Similar to `kraken_2036` but on a WFD footprint of  $24\,700\text{ deg}^2$ .
- `Pontus_2002`: Very large WFD footprint ( $24\,700\text{ deg}^2$ ) and 5 DDFs.
- `pontus_2489`:  $2 \times 15$  s visits replaced by  $1 \times 20$  s in *grizy* and  $1 \times 40$  s in *u* band.
- `pontus_2502`: A rolling cadence (2 dec. bands) in WFD where the baseline cadence stays on at a reward level of 25%.
- `pontus_2506`: Revisits in the same night in different filter.
- `rolling_10yrs_opsim`: A rolling cadence (2 dec. bands) in WFD where the de-emphasized band is set to reach 25% of its usual number of visits in a year; paired visits in *g, r* and *i*.

<sup>7</sup> [https://cadence-hackathon.readthedocs.io/en/latest/current\\_runs.html](https://cadence-hackathon.readthedocs.io/en/latest/current_runs.html) and in addition `pontus_2506` from Tiago Ribeiro.

<sup>8</sup> <http://altsched.rothchild.me:8080/>

<sup>9</sup> [https://github.com/yoachim/SLAIR\\_runs](https://github.com/yoachim/SLAIR_runs)

<sup>10</sup> A discussion within the Dark Energy Science Collaboration revealed that the 3 rolling cadences `kraken_2036`, `mothra_2045` and `pontus_2502` seem to lack some observations. Nevertheless, we inves-

tigate those cadences as all others, because we are mainly interested in the dependency on different parameters. Our statement about rolling cadences would stay the same even if we remove these 3 strategies from our investigation.

- **rolling\_mix\_10yrs\_opsim**: A rolling cadence similar to rolling\_10yrs\_opsim but with revisits in different filters.

### 3.1.2. Categorization of observing strategies

From our investigation (in Section 6), we find that the main relevant parameters for measuring time delays in LSNe Ia are the cumulative season length ( $t_{\text{eff}}$ ), mostly in terms of the total number of LSNe Ia, and the mean inter-night gap ( $t_{\text{gap}}$ ; also referred as sampling frequency or sampling) concerning the quality of the light curves. These two parameters are defined later in this section. For categorizing different observing strategies  $t_{\text{gap}}$  and  $t_{\text{eff}}$  are shown in Figure 5 for 20 LSST observing strategies and from this we can separate them into three different categories with respect to the current LSST baseline cadence strategy (“baseline2018a”):

- **“baseline like”**: baseline-like cadence strategies in terms of sampling/cadence ( $t_{\text{gap}}$ ) and cumulative season length ( $t_{\text{eff}}$ )
- **“higher cadence & fewer seasons”**: higher cadence but shorter cumulative season length
- **“higher cadence”**: higher cadence and baseline-like cumulative season

Readers interested in general properties of the strategies should focus on these 3 categories which are highlighted by the category names and their corresponding colors. Observing strategies in blue “higher cadence & fewer seasons” are all rolling cadences. The alternating observation pattern for different years leads to a shorter cumulative season length and hence an improved sampling. Magenta strategies “higher cadence” provide a better mean inter-night gap than the baseline cadence by reducing the exposure time, doing the revisits of the same field within an hour in different filters or by just doing single visits of a field within a night. For this reason, these strategies provide sampling similar to rolling cadences but they leave the cumulative season length close to the baseline cadence. Rolling cadences which keep the WFD on a 25% reward level have a cumulative seasons length similar to the baseline cadence but do not provide a better mean inter-night gap and are therefore listed in category “baseline like”<sup>11</sup>.

The mean cumulative season length and mean inter-night gap from a simulation of a given observing strategy are calculated by taking the mean of all fields under consideration. We look at two different cases. The first case considers 719 LSST fields from the WFD survey<sup>12</sup>, which is shown as black solid line in Figure 5, with the shaded region marking 99% of the fields. In the second case we consider for comparison all 5292 LSST fields covering the entire sky. We only take into account those fields where observations are taken, which is shown as blue dashed line.

The cumulative season length is the summed up season length over all seasons. A season gap for an LSST field is defined if no observation in any filter is taken for 85 days<sup>13</sup>. The mean cumulative season length of all fields under consideration is shown in the lower panel of Figure 5. For the inter-night gap, shown in the upper panel of Figure 5, the revisits of a field

<sup>11</sup> except for “rolling\_mix\_10yrs\_opsim where the revisit in different filters improves the sampling frequency.

<sup>12</sup> The 719 WFD fields contain all fields with Dec  $\in$   $[-58, -2]$  deg and RA  $\in$   $[0, 120] \cup [330, 360]$  deg, where all DDFs are excluded.

<sup>13</sup> To avoid unrealistically long seasons, we split a season if the season length is longer than 320 days at the biggest gap. Seasons with a season length shorter than 10 days are removed from the simulations.

within hours in the same filter are summarized into a single visit. Because typically SNe do not change over such a short time scale, the data points are combined into a single detection with reduced uncertainty. For some of the observing strategies, the mean inter-night gap between the picked WFD fields deviates significantly from the consideration of all fields, which is due to time spent on other surveys like northern hemisphere, the Southern Celestial pole and the Galactic Center.

## 4. Generating realistic LSST mock light curves of LSNe Ia

The goal of this section is to describe how mock LSST light curves for LSNe Ia are obtained for different cadence strategies. To simulate observations randomly, we use mock LSNe Ia from the OM10 catalog (Oguri & Marshall 2010), where we assume the spherically symmetric SN Ia W7 model (Nomoto et al. 1984) for each image. Synthetic light curves are produced with the radiative transfer code ARTIS (Kromer & Sim 2009) where we include the effect of microlensing via magnifications maps from GERLUMPH (Vernardos et al. 2015, J. H. H. Chan in preparation) following Section 2.3. We then simulate data points for the light curves, following the observation pattern from different cadences and uncertainties according to the LSST science book (LSST Science Collaboration 2009). In Section 4.1 we describe the OM10 mock catalog for strong lenses and Section 4.2 illustrates how we simulate mock light curves for mock LSNe Ia from OM10.

### 4.1. Mock LSNe Ia from the OM10 catalog

The OM10 catalog (Oguri & Marshall 2010) is a mock lens catalog for strongly lensed quasars and supernovae for LSST. For our purpose, we focus on the LSNe Ia in the catalog. We expect about 45 spatially resolved LSNe Ia for the 10-year LSST survey, under the assumption of OM10, namely a survey area of  $\Omega_{\text{OM10}} = 20\,000 \text{ deg}^2$  and a season length of 3 months. The catalog contains LSNe Ia with two images (doubles) and four images (quads), but only those systems, where the multiple images are resolved (minimum image separation of 0.5 arcsec) and where the peak of the i-band magnitude of the fainter image for a double or the 3rd brightest image for a quad falls in an observing season, are in the catalog. The  $10\text{-}\sigma$  point source limiting magnitude in the i band for a single visit is assumed to be 23.3.

The mock catalog assumes as a lens mass model an SIE (Singular Isothermal Ellipsoid; Kormann et al. 1994) and the convergence for the SIE is given in Oguri & Marshall (2010) via

$$\kappa(\theta_1, \theta_2) = \frac{\theta_{\text{Ein}} \sqrt{1-e}}{2} \frac{\lambda(e)}{\sqrt{\theta_1^2 + (1-e)^2 \theta_2^2}}, \quad (16)$$

where  $(\theta_1, \theta_2)$  are the lens coordinates,  $\theta_{\text{Ein}}$  is the Einstein radius in arcsec,  $e$  is the ellipticity and  $\lambda(e)$  the dynamical normalization defined in Oguri et al. (2012). The lens mass distribution is then rotated by its position angle.

The OM10 catalog is composed of two parts. The first part is the input for the SIE model containing properties of the source and the lens, such as redshift, velocity dispersion, source positions and so on. This first part is used to calculate mock images using GLAFIC (Oguri 2010) and therefore predict image positions, magnifications and time delays, which is the second part

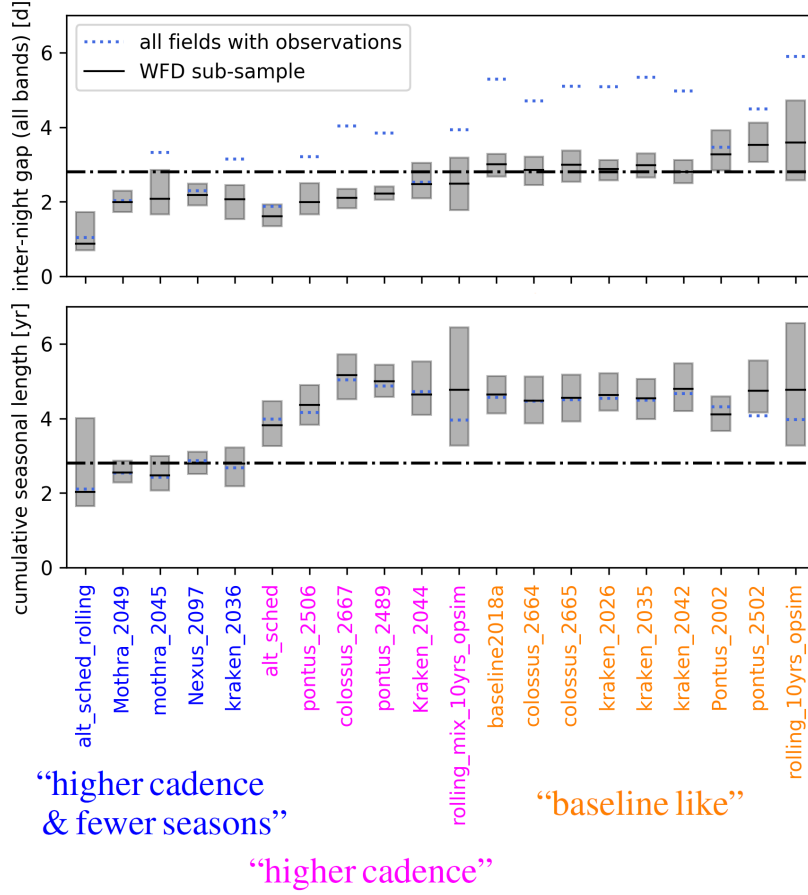


Fig. 5: The mean inter-night gap (upper panel) and mean cumulative season length (lower panel) for 20 different observing strategies for two cases. The first case (“WFD” in solid black) considers 719 LSST fields, which all lie in the WFD survey. The shaded region encloses the 99th percentile of the WFD fields. The second case (“all” in dotted blue) considers all of the 5292 LSST fields where observations are taken and is just shown for comparison. In the upper panel, cadences with the black solid line below the black dot-dashed line are those with a significantly better inter-night gap than the baseline cadence (i.e., magenta “higher cadence” and blue “higher cadence & fewer seasons” strategies), whereas the others are baseline-like (orange “baseline like”). From the lower panel we distinguish between strategies with a cumulative season length similar to the baseline cadence (magenta “higher cadence” and orange “baseline like”) and a significantly worse cumulative season length (blue “higher cadence & fewer seasons”).

of the OM10 catalog. To get the macro and microlensing magnification for different images, a microlensing map like the one in Figure 1 is needed and therefore  $\kappa$  and  $\gamma$  have to be known for each of the mock images<sup>14</sup>. We calculate these parameters analytically for the SIE model following equations from Kormann et al. (1994), Oguri & Marshall (2010) and Oguri et al. (2012), and check the consistency by comparing to magnification factors predicted by GLAFIC.

The distribution of the source redshift and the time-delay of all OM10 mock systems is shown in Figure 6. For quad systems, the maximum of the 6 possible time delays (between pair of images) is shown. All 417 LSNe Ia from OM10 correspond to the blue line. To reduce the computational effort for the investigations in Section 6 we restrict ourselves to a sub-sample of 202 mock LSNe Ia (101 mock quads and 101 mock doubles) which is represented by the orange line. We find LSNe Ia for a source redshift of 0.2 to 1.4 where most of them are around 0.8. In terms of time delays, most of the systems have a maximum delay shorter than 20 days. There are only a few systems with very long time delays (greater than 80 days).

<sup>14</sup> In principle also the smooth matter fraction  $s$  but for simplicity we assume as before  $s = 0.6$ .

#### 4.2. Sampling of the light curves for various LSST observing strategies

To simulate observations, we randomly pick 202 mock LSNe Ia from the OM10 catalog (see orange curves in Figure 6) and produce synthetic microlensed light curves for the mock SNe images following Section 2.3. As an example a mock quad system and the corresponding light curves (each image in a random position in its corresponding microlensing map) is shown in Figure 7. Image A arrives first followed by C, D and B. In the simulated light curves of image D (red solid line), an ongoing microlensing event is visible as additional brightening about 80 d after the peak, which is not visible in the other three images.

To get simulated data points from the theoretical light curves as shown in Figure 7, we have to combine the light curves with an observing sequence of visits. This is illustrated for the “baseline2018a” cadence in Figure 8 where for one field in the WFD, all observations within the 10-year survey are shown. For this purpose, we pick 10 fields in the WFD survey which

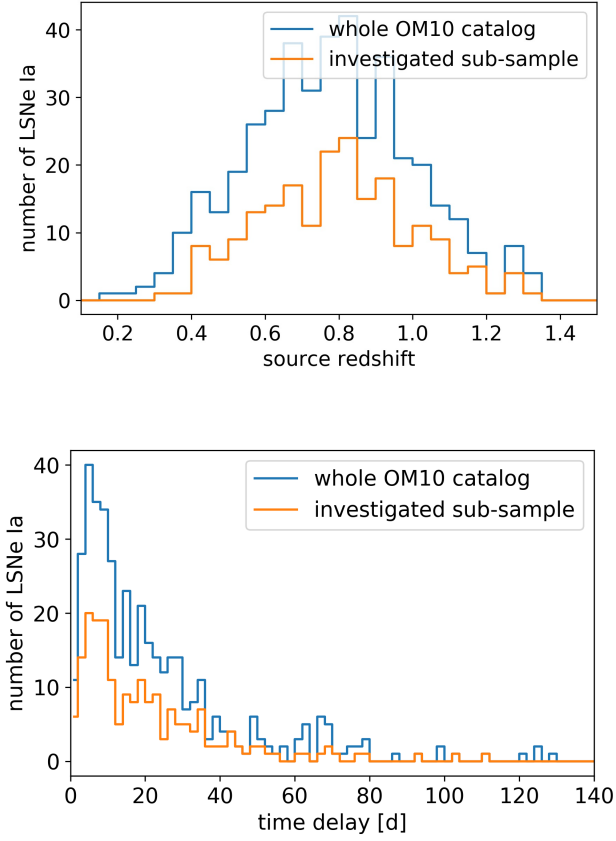


Fig. 6: Source redshift (upper panel) and time-delay (lower panel) distribution of LSNe Ia from the OM10 catalog. The blue line shows the whole catalog (417 mock systems). The orange line shows the sub-sample of 202 mock systems (101 randomly picked quads and 101 randomly picked doubles) under investigations in Section 6. For the time-delay distribution, the maximum time delay is shown (just relevant for quads) and there are three systems not in the plot with time delays greater than 140 days. The highest delay of a LSNe Ia in the OM10 catalog is 290 days.

are listed in Table 1<sup>15</sup>. That these 10 fields are representative for the WFD survey is shown in Figure 9. Here the mean inter-night gap (top left panel), mean cumulative season length (bottom left panel) and mean  $5\sigma$ -depth for bands  $g$  (top right panel) and  $r$  (bottom right panel) for our 10 fields (orange), WFD fields (black) and all fields (blue) are shown, while the shaded region encloses the 99th percentile.

For each of the 10 fields for a given cadence, we consider the following for each visit of the field: date (mjd), filter(s) observed, and  $5\sigma$  point-source depth  $m_5$ . The depth is needed to calculate the photometric uncertainties  $\sigma_1$  according to the LSST Science Collaboration (2009) (see Appendix B). The magnitude for each data point can then be calculated via

$$m_{\text{data}} = m_{W7} + r_{\text{norm}}\sigma_1, \quad (17)$$

where  $r_{\text{norm}}$  is a random number following the normal distribution and  $m_{W7}$  is the magnitude of the data point from the theoretical W7 model. By placing the synthetic light curves (shown as

<sup>15</sup> We do not add dithering to observing strategies simulated with the OpSim scheduler, which means that we underestimate the number of visits slightly.

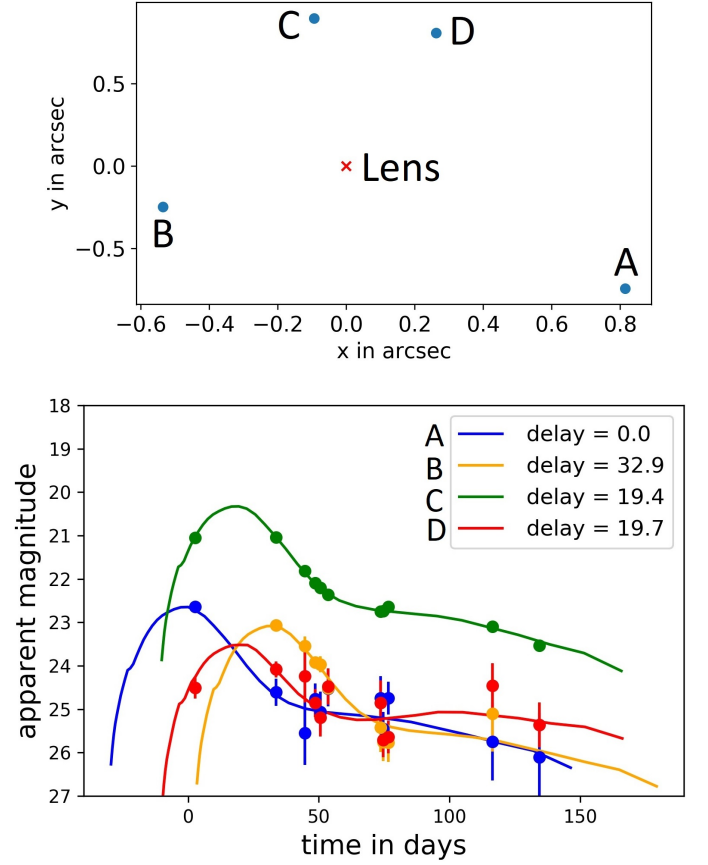


Fig. 7: Synthetic  $i$ -band light curves (lower panel) of a mock quad LSNe Ia (upper panel) to illustrate simulated observations. The redshift of the source is 0.71 and is taken into account. The observation sequence is for a random field in the WFD survey for the “baseline2018a” cadence.

solid lines in Figure 7) randomly in one of the fields in Table 1, randomly in time such that the detection criteria from the OM10 catalog is fulfilled, and using Equation (17), we create simulated data points as illustrated in Figure 7. If two or more data points are taken within one hour in the same filter we combine them into a single measurement, because SNe typically do not change on such time scales. Specifically, two data points  $m_{\text{data},1} + \sigma_1$  and  $m_{\text{data},2} + \sigma_2$  observed at time  $t_1$  and  $t_2$ , where  $t_1 \leq t_2 \leq t_1 + 1$  h, are combined into a single one as

$$m_{\text{combined}} + \sigma_{\text{combined}}, \quad (18)$$

where

$$m_{\text{combined}} = \frac{m_1/\sigma_1^2 + m_2/\sigma_2^2}{1/\sigma_1^2 + 1/\sigma_2^2}, \quad \sigma_{\text{combined}} = \sqrt{\frac{1}{1/\sigma_1^2 + 1/\sigma_2^2}}. \quad (19)$$

We assign to the combined data point the time  $t_{\text{combined}} = (t_1 + t_2)/2$ .

## 5. Time-delay measurements

In this section we describe how we estimate time-delays from the simulated observations to quantify different observing strategies. To have sufficient statistics, we investigate 202 mock LSNe Ia (already mentioned in Section 4) for each cadence strategy, where we pick 50% doubles and 50% quads. We define a system with “good” time delay measurement as a systems where

field number	1	2	3	4	5	6	7	8	9	10
RA in deg	0.0	32.1	65.8	50.9	44.9	125.6	155.0	207.7	304.3	327.5
DEC in deg	-7.4	-44.2	-7.2	-30.0	-50.9	-11.4	-25.6	-45.3	-55.2	-35.9

Table 1: The 10 fields of the WFD survey, where the observational sequence for different cadences is considered, which is used to determine the fraction of systems with measured time delay as discussed in Section 6. We investigate the observing sequence at the centers of the listed fields.

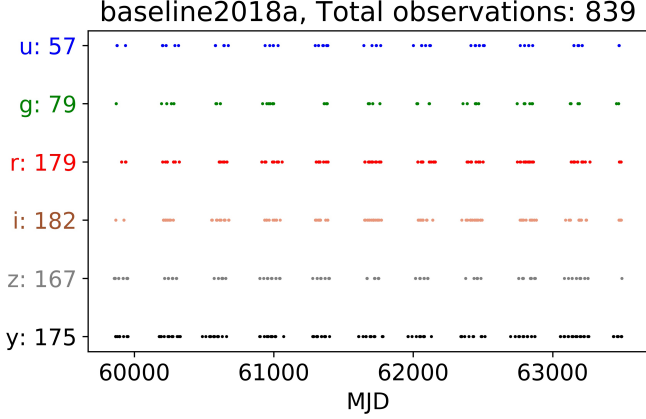


Fig. 8: As an example this illustrates the Modified Julian Date (MJD) and filters when observations are taken over the 10-year survey for field number 4 from Table 1 for the observing strategy “baseline2018a”. The y axis shows the 6 LSST filters and the number of observations taken in that filter.

the accuracy is below 1% and the precision is below 5%. To estimate accuracy and precision we investigate for each of the mock systems, 100 random starting configurations. A starting configuration corresponds to a random position in the microlensing map and a random field from Table 1, where it is placed randomly in one of the observing seasons such that the detection requirement from OM10 is fulfilled. To avoid uncertainties due to different microlensing patterns, we use the same random positions for each mock image for all observing strategies investigated here. For each of these starting configurations, we then draw 1000 different noise realizations of light curves following Equation (17). For each of these realizations we have to estimate the time delay and compare it to the true value.

To get a measured time delay from the mock data we use the free-knot splines estimator from PyCS (Python Curve Shifting; Tewes et al. 2013; Bonvin et al. 2016). As a spline, a piecewise polynomial function of degree 3 is used. The polynomial pieces are connected by knots, where for the optimization process, the initial number of knots has to be specified. The polynomial coefficients and the knot positions are free variables to optimize. To avoid clustering of the knots a minimum knot separation is also defined in advance (Molinari et al. 2004). The basic idea of the optimizer is to fit a single intrinsic spline to two light curves from different images and shift the data iteratively in time and magnitude, and modify the spline parameters, to get a time-delay measurement. We show in Figure 10 an example of the fitting of the spline to two light curves, with one light curve time-shifted by the time delay to increase overlap with the other. Both the spline parameters and the time delay between the two curves are optimised by reducing the residuals in the fit of the spline to the two light curves. Even with noiseless data, we would get a spread of delays from PyCS due to the range of splines that

could fit to the data equally well. Densely sampled light curves with little microlensing would restrict the range of delays. We do not explicitly include additional spline components to model the microlensing variation. An analysis that models separately the intrinsic and microlensing variability is deferred to future work.

PyCS was initially developed to measure time delays in strongly lensed quasars, and is not yet optimized for LSNe Ia, such as fitting simultaneously multiple filters and using SN template light curves. Nonetheless, Rodney et al. (2016) used the tools of PyCS to measure the time delays between the multiple images of SN Refsdal as one of the approaches, and also fitted SN templates to the light curves as another other approach. The resulting delays from both approaches were consistent with each other. While both methods did not explicitly include the effects of microlensing, the residuals of the light curves of SN Refsdal suggested that no major microlensing event occurred in the case of SN Refsdal (Rodney et al. 2016). The template-fitting approach was also used by Goldstein et al. (2018b) to fit to mock light curves and color curves, although in an idealized scenario without noise and high-cadence sampling. Goldstein et al. (2018b) found the fitting of templates to light curves yielded time-delay uncertainties of  $\sim 4\%$ , limited by microlensing distortion of light curves, whereas the fitting to color curves in the achromatic phase provided  $\sim 1\%$  uncertainties in the delays. For our LSST light curves, we opt to use PyCS on light curves given that (1) color curves are not available from LSST data given the sampling cadence, and (2) there is currently no publicly available template-fitting software accounting for microlensing, an effect that can significantly distort the light curves as shown in Section 2.

Applying PyCS to individual filter’s light curves, we get a single independent time delay for each filter. This means that we have for the given LSST filter  $f$ , the  $j$ -th starting configuration and the  $k$ -th noise realization a deviation from the true time delay:

$$\tau_{d,f,j,k} = \frac{\Delta t_{\text{measured},f,j,k} - \Delta t_{\text{true},f,j,k}}{\Delta t_{\text{true},f,j,k}}. \quad (20)$$

For each observing strategy and double LSNe Ia, we have thus 1 (delay for the one pair of images)  $\times$  6 (filters)  $\times$  100 (starting configurations)  $\times$  1000 (noise realisations) time-delay deviations as in Equation (20). For the 6 pairs of images for a quad system, we have a sample of  $6 \times 6 \times 100 \times 1000$ .

To exclude starting configurations which are completely wrong in comparison to most of the investigated systems we first calculate separately for *each* starting configuration the median  $\tau_{d,50,f,j}$  and the error as  $\delta_{f,j} = (\tau_{d,84,f,j} - \tau_{d,16,f,j})/2$ , where  $\tau_{d,50,f,j}$ ,  $\tau_{d,84,f,j}$  and  $\tau_{d,16,f,j}$  are the 50th, 84th and 16th percentile from the 1000 noise realizations. Further we combine the 6 filters via the weighted mean into a single time-delay deviation  $\tau_{d,50,j} \pm \delta_j$ , where

$$\tau_{d,50,j} = \frac{\sum_{f=ugrizy} \tau_{d,50,f,j} / \delta_{f,j}^2}{\sum_{f=ugrizy} 1 / \delta_{f,j}^2}, \quad \delta_j = \sqrt{\frac{1}{\sum_{f=ugrizy} 1 / \delta_{f,j}^2}}. \quad (21)$$

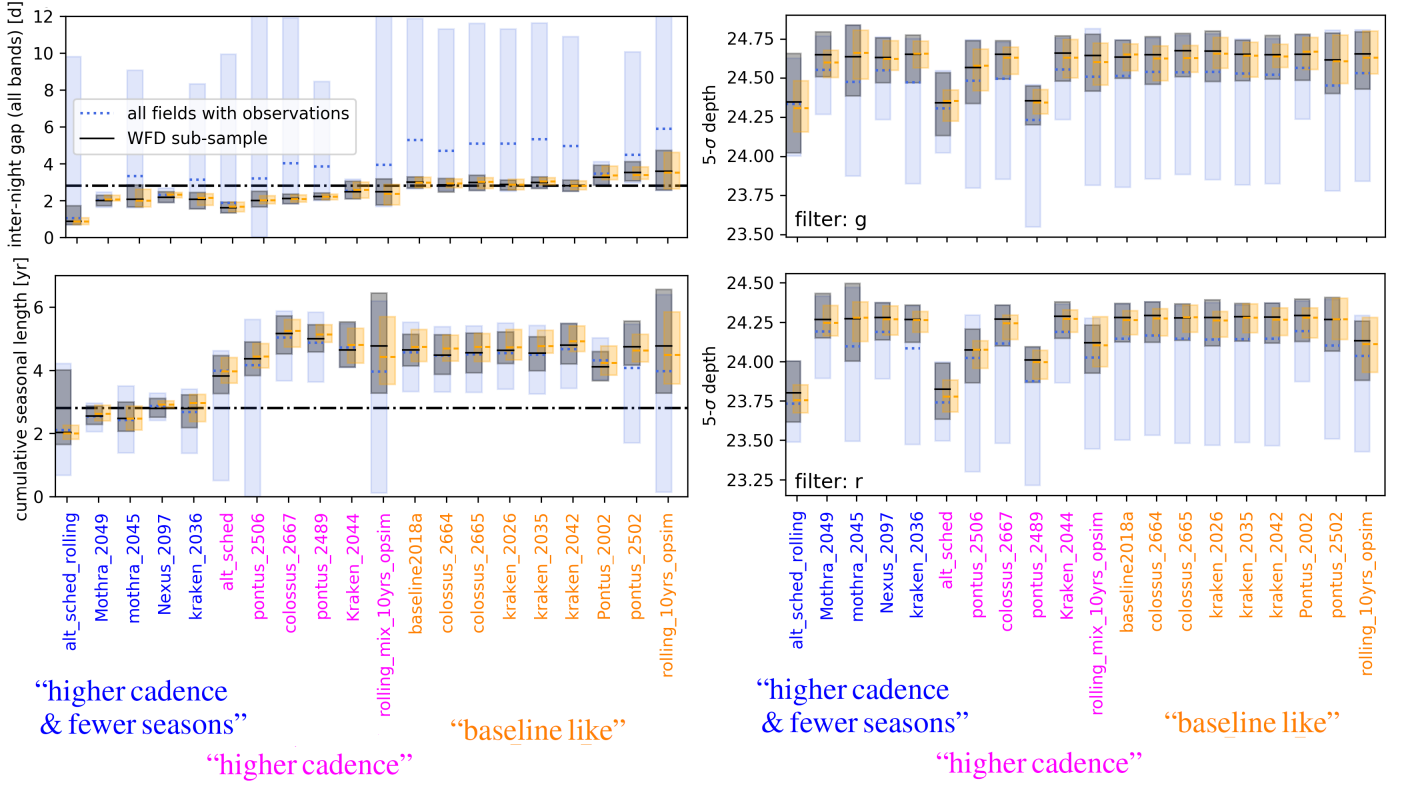


Fig. 9: Comparison of the inter-night gap, cumulative season length and  $5\sigma$ -depth of the 10 fields under investigation (orange) to the sample of 719 WFD (black) fields. In addition, all 5292 LSST fields where observations are taken (blue) are shown. The lines indicate the mean and the shaded area includes everything up to the 99th percentile. We see that the 10 chosen fields are representative for the WFD survey but not for the whole survey.

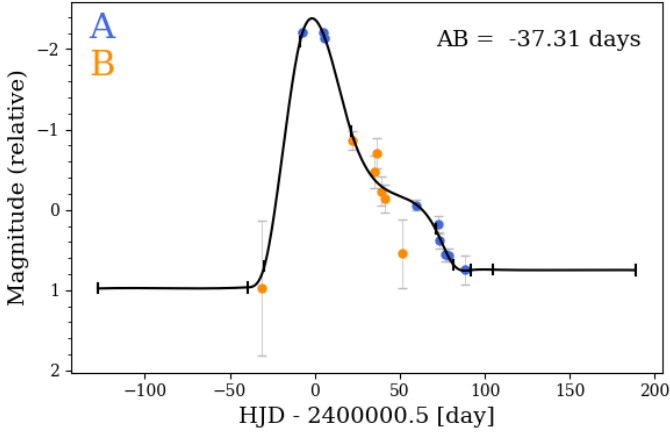


Fig. 10: Illustration of the spline fitting technique for a double mock LSNe Ia at redshift 0.27 for the  $i$ -band light curve. The black line corresponds to the spline fit of the data (blue and orange), where the knots positions (small vertical ticks on the black lines) as well as the magnitude and time shifts have been iteratively optimized to minimize a chi-square term, resulting in the measured delay indicated in the top-right.

This is possible since the distribution of the time-delay deviation for each filter is approximately Gaussian. From this we exclude “catastrophic failures” which are starting configurations with  $\delta_j \geq 2\delta_j$  or  $|\tau_{d,50,j} - \bar{\tau}_{d,50,j}| \geq 5\delta_j$ , which occur for about

10% of the starting configurations independent of the observing strategy. The bar indicates the mean, i.e.,

$$\bar{\delta}_j = \frac{1}{100} \sum_{j=1}^{100} \delta_j \quad \text{and} \quad \bar{\tau}_{d,50,j} = \frac{1}{100} \sum_{j=1}^{100} \tau_{d,50,j}. \quad (22)$$

The failures are likely due to a bad starting time of the supernova in the season (such as at the beginning or end of season, where some of the light curves of the multiple images would be incomplete due to seasonal gap) and strong microlensing distortions. These effects could be easily identified in real lens systems, and provide advance warning of potentially problematic delay inference. In addition, simulations of light curves mimicking those of real lens systems could be used to identify catastrophic failures of problematic systems and avoid the use of their time delays for further analysis such as cosmography.

After excluding “catastrophic failures” we are left with about 90 of the 100 initial starting configurations leading to  $\sim 90 \times 1000 \approx 90000$  time-delay deviations  $\tau_{d,f,j,k}$  for each filter  $f$ . From these we define accuracy as the median  $\tau_{d,50,f}$  and precision as  $\delta_f = (\tau_{d,84,f} - \tau_{d,16,f})/2$ , where  $\tau_{d,84,f}$  is the 84th and  $\tau_{d,16,f}$  the 16th percentile of the 90000 starting configuration and noise realizations, i.e., over the  $j$  and  $k$  indices. Since the time-delay deviations from the 6 filters are independent, we combine them into a single time-delay deviation. This means that in the end, we have for one strategy and a mock LSNe Ia a single  $\tau_{d,50} \pm \delta$  per pair of images, where

$$\tau_{d,50} = \frac{\sum_{f=\text{ugrizy}} \tau_{d,50,f}/\delta_f^2}{\sum_{f=\text{ugrizy}} 1/\delta_f^2}, \quad \delta = \sqrt{\frac{1}{\sum_{f=\text{ugrizy}} 1/\delta_f^2}}. \quad (23)$$

To use the weighted mean here is possible since the time-delay distributions for different filters are approximately Gaussian.

## 6. Results: cadence strategies for LSNe

In this section, we present the results of the investigation of the different cadence strategies presented in Section 3. We distinguish between two different cases: (1) using LSST data only for measuring time delays, and (2) using LSST just as a discovery machine for LSNe Ia and getting the time delay(s) from follow-up observations.

Given that  $H_0 \propto \Delta t_{\text{true}}^{-1}$ , where  $\Delta t_{\text{true}}$  is the time delay between two images, we aim for accuracy ( $\tau_{d,50}$  in Equation (23)) smaller than 1% and precision ( $\delta$  in Equation (23)) smaller than 5%. We refer to systems fulfilling these requirements as systems with “good” time delays. A quad system is counted as successful if at least one of the 6 delays fulfills these demands. The accuracy requirement is needed for measuring  $H_0$  with 1% uncertainty, and the precision requirement ensures that the delay uncertainty does not dominate the overall uncertainty on  $H_0$  given typical mass modeling uncertainties of  $\sim 5\%$  (e.g., Suyu et al. 2018).

### 6.1. Number of LSNe Ia

Before comparing cadence strategies based on the time-delay measurements, we first estimate the total number of LSNe Ia for different observing strategies. Since different observing strategies have different survey areas and different cumulative season lengths, the number of LSNe Ia deviates from the predicted number from OM10. We approximate the total number of LSNe Ia as

$$N_{\text{LSNeIa,cad}} \approx N_{\text{LSNeIa,OM10}} \frac{\Omega_{\text{cad}}}{\Omega_{\text{OM10}}} \frac{\bar{t}_{\text{eff,cad}}}{t_{\text{eff,OM10}}}, \quad (24)$$

where  $N_{\text{LSNeIa,OM10}} = 45.7$ ,  $\Omega_{\text{OM10}} = 20\,000 \text{ deg}^2$  and  $t_{\text{eff,OM10}} = 2.5 \text{ yr}$  from Oguri & Marshall (2010).  $\bar{t}_{\text{eff,cad}}$  is the effective/cumulative season length for a given cadence strategy, where we have averaged over the sample of 719 WFD fields.  $\Omega_{\text{cad}}$  is the survey area for a given observing strategy. Instead of taking the nominal values (24 700  $\text{deg}^2$  for large footprint strategies and 18 000  $\text{deg}^2$  for rest) we calculate the area from fields represented by our study, which are the fields with a mean cumulative season length and inter-night gap similar or even better than the 719 WFD fields, i.e., cumulative season length ( $t_{\text{eff}}$ ) longer than the lower 99th percentile and inter-night gap ( $t_{\text{gap}}$ ) shorter than the upper 99th percentile. Further we also take into account the  $5\sigma$  depth ( $m_5$ ), where we consider only the main relevant bands  $g,r,i$  and  $z$ . Here we consider all fields with ( $m_5 + 0.2 \text{ mag}$ ) greater than the lower 99th percentile of the 719 WFD fields. The relaxed  $5\sigma$  depth is necessary in order to represent the wider areas as suggested by the nominal values<sup>16</sup>. The area can then be calculated from the number of fields fulfilling the above defined criteria ( $N_{\text{cad,criteria}}$ ), multiplied with the field of view of 9.6  $\text{deg}^2$ , taking into account the overlap factor of the fields:

$$\Omega_{\text{cad}} = f_{\text{overlap}} \cdot N_{\text{cad,criteria}} \cdot 9.6 \text{ deg}^2, \quad (25)$$

<sup>16</sup> This leads to a few percent overestimation of the total number of LSNe Ia with “good” time delays for large footprints in comparison to the 18 000  $\text{deg}^2$ . Nonetheless, since we find that the improvement due to wider area is too small this is not a problem and does not affect the overall conclusions of our work.

	$N_{\text{LSNeIa,cad}}$	$\bar{t}_{\text{eff,cad}}$ in yr	$\Omega_{\text{cad}}$ in $\text{deg}^2$
Kraken.2044	101.9	4.64	24010
Pontus.2002	86.0	4.11	22926
colossus.2667	84.0	5.16	17797
pontus.2489	81.1	5.00	17758
rolling.10yrs.opsim	79.1	4.77	18148
rolling.mix.10yrs.opsim	78.9	4.76	18132
kraken.2042	78.0	4.79	17828
colossus.2665	76.8	4.55	18475
pontus.2502	76.3	4.74	17602
colossus.2664	74.6	4.48	18202
baseline2018a	73.4	4.64	17306
kraken.2035	73.4	4.54	17680
kraken.2026	72.4	4.63	17119
pontus.2506	72.2	4.36	18132
alt.sched	61.7	3.81	17703
Nexus.2097	52.2	2.79	20471
Mothra.2049	50.9	2.55	21874
kraken.2036	45.2	2.79	17719
alt.sched.rolling	37.9	2.03	20463
mothra.2045	37.2	2.48	16417

Table 2: Total number of LSNe Ia over the 10-year survey calculated via equation (24) where 69% are doubles and 31% are quads. To understand the differences between the multiple strategies also the cumulative season length  $\bar{t}_{\text{eff,cad}}$  and the survey area  $\Omega_{\text{cad}}$  are shown. The total number depends on the selection criteria assumed in Oguri & Marshall (2010). If we relax the criteria like the image separation these numbers will be higher, but the order will be unchanged.

where

$$f_{\text{overlap}} = \frac{4\pi \cdot (180 \text{ deg}/\pi)^2}{5292 \cdot 9.6 \text{ deg}^2} \approx 0.812. \quad (26)$$

5292 are the total number of fields covering the entire sky, as noted in Section 3.1 and the numerator corresponds to the surface area of a sphere in  $\text{deg}^2$ .  $\Omega_{\text{cad}}$  is therefore equivalent to  $4\pi N_{\text{cad,criteria}}/5292$  in units of  $\text{rad}^2$ . The results from Equation (24) for the 20 investigated cadences are shown in Table 2. We find that mainly the cumulative season length sets the order of the table and therefore for rolling cadences with a lower number of observing seasons (blue “higher cadence & fewer seasons” strategies) many LSNe Ia will not be detected, because of the alternating observation scheme.

### 6.2. LSST data only

Here, we quantify the 20 investigated cadences for the case of using LSST data only for measuring time delays. We have investigated 101 randomly picked quads and 101 randomly picked doubles. The distribution of the source redshifts and time delays are shown as orange lines in Figure 6. The 202 systems are used to determine the fraction  $f_a$  of systems with “good” time delays:

$$f_a = \frac{N_{\Delta t,a}}{N_a} \quad a = \text{double, quad}, \quad (27)$$

where  $N_{\Delta t,a}$  is the number of systems with “good” time delays and  $N_a = 101$  for  $a = \text{double, quad}$ . Since we have picked the same amounts of doubles and quads, whereas the real ratio between doubles and quads in the OM10 catalog is 69 : 31, the total fraction can be calculated as

$$f_{\text{total}} = 0.69 f_{\text{double}} + 0.31 f_{\text{quad}}. \quad (28)$$

The fractions of doubles  $f_{\text{double}}$  and quads  $f_{\text{quad}}$  as well as the total fraction  $f_{\text{total}}$  are shown in Table 3. It becomes clear that the fraction of systems with good delays depends mostly on the inter-night gap, where strategies with better sampling (blue “higher cadence & fewer seasons” and magenta “higher cadence” strategies) provide higher fractions.

	$f_{\text{total}}$	$f_{\text{double}}$	$f_{\text{quad}}$
alt_sched_rolling	17.2	21.8	6.9
alt_sched	13.5	17.8	4.0
rolling_mix_10yrs_opsim	10.2	13.9	2.0
pontus_2506	9.1	11.9	3.0
colossus_2667	9.1	11.9	3.0
pontus_2489	7.4	9.9	2.0
rolling_10yrs_opsim	6.8	8.9	2.0
mothra_2045	6.1	7.9	2.0
Kraken_2044	5.8	7.9	1.0
kraken_2042	5.8	7.9	1.0
Nexus_2097	4.8	6.9	0.0
kraken_2026	4.8	6.9	0.0
Mothra_2049	4.7	5.9	2.0
kraken_2036	4.7	5.9	2.0
colossus_2665	3.7	5.0	1.0
baseline2018a	3.7	5.0	1.0
colossus_2664	3.4	5.0	0.0
kraken_2035	2.0	3.0	0.0
pontus_2502	1.4	2.0	0.0
Pontus_2002	1.4	2.0	0.0

Table 3: Fraction of systems (in %) of the 202 investigated mock systems (101 doubles and 101 quads) where the time delay has been measured with accuracy smaller than 1% and precision smaller than 5% for the case of using LSST data only.  $f_{\text{total}}$  accounts for the expected 69:31 ratio of doubles and quads from OM10 (see Equation (28)). The investigation has been done for the 10 fields listed in Table 1. These are not the final results as the total number of detected LSNe Ia is not taken into account.

To determine the value of a given cadence strategy for our science case, we combine Table 2 and 3. The results for the 10-year survey are shown in Figure 11. One sees that the key for obtaining a high number of LSNe Ia with good delays is *short inter-night gap while keeping the cumulative season length baseline-like* (magenta “higher cadence” strategies). Only for the strategy “alt\_sched\_rolling”, the much better sampling can compensate for the short cumulative season length.

From the upper panel of Figure 12, it becomes clear that only nearby systems ( $z \lesssim 0.9$ ) with long time delays ( $\Delta t \gtrsim 25$  d) are measured successfully. High redshift systems are overall fainter and the larger photometric errors make delay measurements more uncertain. Shorter time delays are not accessible because of the sparse sampling and microlensing uncertainties. Looking at the total number in Figure 11, we find that even the best strategies provide just a handful of systems and therefore using just LSST data for measuring time delays is not ideal. Therefore we investigate the prospects of using follow-up observations in combination with LSST data.

### 6.3. LSST + follow-up observation

Here, we investigate 20 different LSST observing strategies for using LSST just as a discovery machine. To get the time delay we assume follow-up observation in the 3 filters  $g$ ,  $r$  and  $i$ , going to a depth of  $m_{5,g} = 24.60$  mag,  $m_{5,r} = 24.23$  mag and  $m_{5,i} = 23.67$  mag, which are similar to the depth of the base-

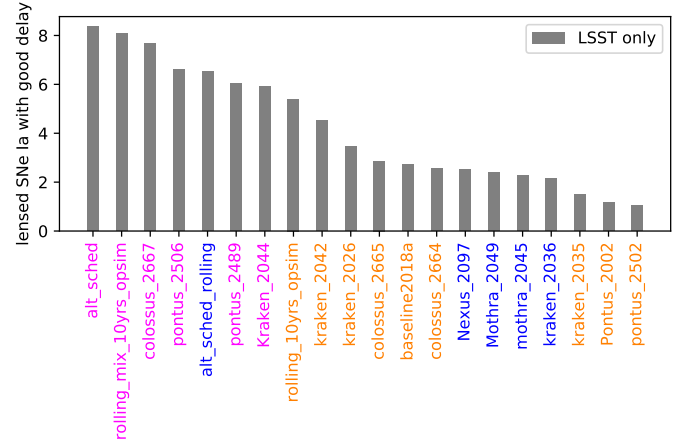


Fig. 11: Number of LSNe Ia for the 10-year survey where the time delay has been measured with accuracy < 1% and precision < 5% for using only LSST data.

line cadence. These depths correspond to an observing time of  $\sim 6$  min per filter and night on a 2 m telescope, which is despite diameter assumed to be identical to LSST (e.g. detector sensitivity). We adopt a realistic scenario where follow-up starts two days after the third data point exceeds the  $5\sigma$  depth in any filter<sup>17</sup>. The follow-up is assumed to take place every second night in all 3 filters. Alternative follow-up scenarios are investigated in Section 6.4.

Assuming a 2-meter telescope is a conservative assessment of the follow-up resources. Observing with larger telescopes would be quite reasonable, which would significantly reduce the exposure time or enable greater depth. The prospects of deeper follow-up will be discussed in Section 6.4.

The fraction of systems with well measured time delays is calculated similar to Section 6.2 and summarized in Table 4 for the 20 investigated observing strategies. Applying only the accuracy requirement ( $\tau_{d,50} < 1\%$ ) would yield for all cadence strategies about 30% less systems from the 202 investigated ones with a slight trend for more accurate systems for cadence strategies with improved sampling. Since for the case of “LSST + follow-up” accuracy is only weakly dependent on the cadence strategy, the precision requirement ( $\delta < 5\%$ ) sets mostly the order of Table 4. Since blue (“higher cadence & fewer seasons”) and magenta (“higher cadence”) strategies perform better than orange (“baseline like”) strategies in Tables 3 and 4, we see that for a good precision a short inter-night gap is important. Even though the light curves for Table 4 are created via follow-up resources, the better inter-night gap is still important to detect systems earlier and get better sampled light curves, although it is less important as for “LSST only” where the ratio between the best and worst cadence strategy is  $\sim 12$  instead of  $\sim 2$  for “LSST + follow-up”. This makes clear that in terms of the fraction of systems with good delays, the sampling is still important but far less than if we would rely on LSST data only. From Table 4 we see that we can increase the fraction and therefore the number of LSNe Ia with good delays for “LSST + follow-up” in comparison to using only LSST data by a factor of 2 to 16, depending on

<sup>17</sup> Goldstein et al. (2018a) suggests that follow-up after 3 data points might be optimistic, but we would like to point out that this relies on the applied classification scheme (Goldstein et al. 2018b) that does not make use of all available lensing information which would help with identification.

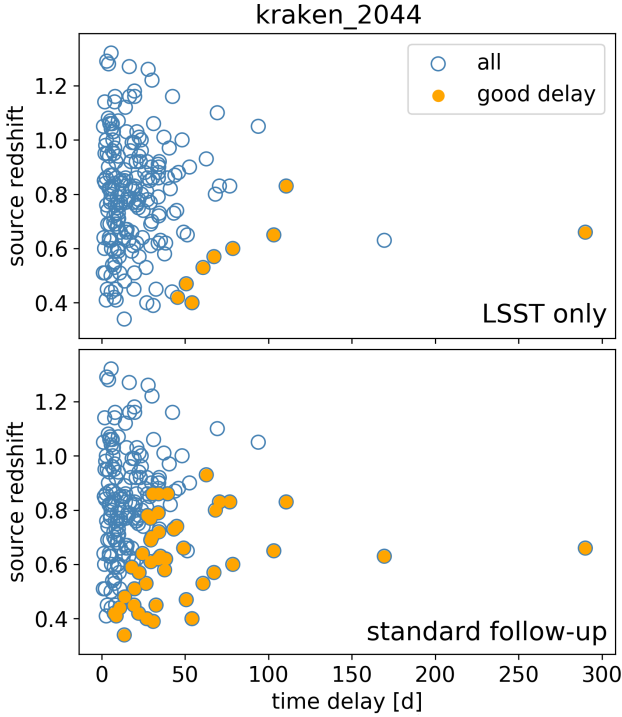


Fig. 12: Time-delay and source-redshift distribution for the 202 investigated mock LSNe Ia for “LSST only” (upper panel) and “LSST + follow-up” (lower panel) for the observing strategy `kraken_2044`. For a quad system, just a single delay is shown, either the first successful measured time-delay or the maximum of the 6 possible time delays. The blue circles show all 202 investigated systems and the orange filled dots correspond to systems where the time delay has been measured with accuracy better than 1% and precision better than 5%. Comparing the two panels we see significant improvement going from “LSST only” to “LSST + follow-up”, which we find for most of the observing strategies as suggested by Table 4. However, for a few cadence strategies (e.g. “`alt_sched_rolling`”) the effort of triggering follow-up might be questionable.

the cadence strategy. For a strategy like “`alt_sched_rolling`”, the effort of triggering the above defined follow-up observation is questionable, but for most other strategies the improvement is significant.

In practice it is important to pick systems with good accuracy for a final cosmological sample in order to determine  $H_0$ . We find that the reduction due to our accuracy requirement is partly due to microlensing but also the quality of the light curve plays a role since follow-up with greater depth provide more systems with accurate time delays. The prospects of greater depth are investigated in Section 6.4 and one way to mitigate the effect of microlensing is the use of the color information as discussed in Appendix A. From Figure 13 we see that for “LSST + follow-up” nearly all time delays greater than 20 days yield an accuracy within one percent, whereas going for short delays is dangerous in terms of adding bias to a final cosmological sample.

In the lower panel of Figure 12, we see that similar to the case of using only LSST data, we are limited to nearby systems ( $z \lesssim 0.9$ ). In terms of time delays, we can reach lower values due to the much better quality of the light curve, but still, most of the short time delays are not accessible because of microlensing and our cut on precision.

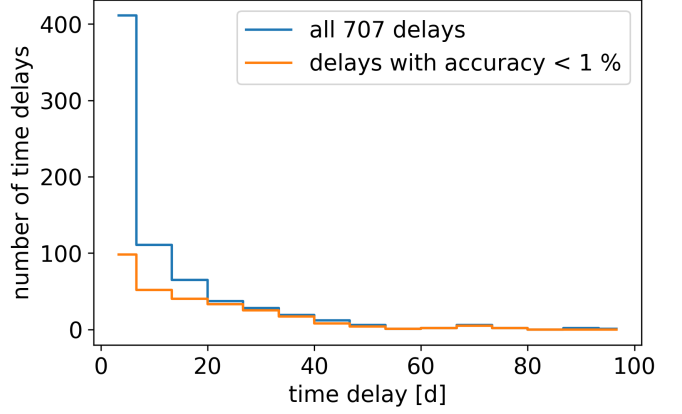


Fig. 13: Duration distribution for all 707 possible time delays (blue) and time delays with accuracy better than 1% (orange) from the 202 investigated systems (101 double and 101 quads) for “LSST + follow-up” and the observing strategy “`colossus_2667`”. Nearly all time delays are accurate for pairs of images which yield a time delay greater than 20 days.

	$f_{\text{total}}$	$f_{\text{double}}$	$f_{\text{quad}}$	$\frac{f_{\text{total,LSST+follow-up}}}{f_{\text{total,LSSTonly}}}$
<code>alt_sched_rolling</code>	34.4	43.6	13.9	2.0
<code>alt_sched</code>	32.1	41.6	10.9	2.4
<code>colossus_2667</code>	31.1	40.6	9.9	3.4
<code>pontus_2506</code>	27.0	34.7	9.9	3.0
<code>mothra_2045</code>	26.7	35.6	6.9	4.4
<code>Kraken_2044</code>	26.7	34.7	8.9	4.6
<code>kraken_2042</code>	25.0	32.7	7.9	4.3
<code>kraken_2026</code>	24.3	31.7	7.9	5.1
<code>kraken_2036</code>	24.0	31.7	6.9	5.1
<code>pontus_2489</code>	23.6	30.7	7.9	3.2
<code>Mothra_2049</code>	23.6	30.7	7.9	5.0
<code>rolling_mix_10yrs_opsim</code>	23.3	30.7	6.9	2.3
<code>Nexus_2097</code>	23.3	30.7	6.9	4.9
<code>baseline2018a</code>	23.3	30.7	6.9	6.3
<code>Pontus_2002</code>	22.0	28.7	6.9	16.1
<code>kraken_2035</code>	22.0	28.7	6.9	10.7
<code>colossus_2665</code>	22.0	28.7	6.9	5.9
<code>colossus_2664</code>	22.0	28.7	6.9	6.4
<code>pontus_2502</code>	20.3	26.7	5.9	14.8
<code>rolling_10yrs_opsim</code>	18.2	23.8	5.9	2.7

Table 4: Fraction of systems (column 2, 3 & 4 in %) of the 202 investigated mock systems (101 doubles and 101 quads) where the time delay has been measured with accuracy smaller than 1% and precision smaller than 5% for the case of using LSST as a discovery machine and getting time delays from follow-up observations. The investigation has been done for the 10 fields listed in Table 1. The 5th column shows how much better a cadence performs in comparison to using LSST data only. This table is insufficient to rank different cadence strategies because the total number of detected LSNe Ia is not taken into account.

By combining Tables 2 and 4, we get the total amount of LSNe Ia with good time delays as shown in Figure 14. We note here that the presented results have errors within 10% due to uncertainties in the calculated area and sampling. While this might change the ordering slightly, it does not influence our overall conclusions which will be presented in the following.

We see that for the current baseline strategy we would expect  $\sim 17$  LSNe Ia with good delays over the 10-year survey. To in-

crease this number, the most promising strategies are those with a baseline-like cumulative season length  $\bar{t}_{\text{eff,cad}}$  and an enhanced sampling (magenta “higher cadence” strategies). To achieve this, the most efficient way would be to get rid of the revisit within the same night (compare “colossus\_2667” to “baseline2018a”). Because this would make the science case of fast moving objects impossible, we think a reasonable compromise is to do the revisit within the same night in a different filter (Lochner et al. 2018). This performs worse than doing single visits but still better than doing the revisit in the same filter (compare “pontus\_2506” to “colossus\_2667” and “baseline2018a”). In terms of the cumulative season length, it seems appropriate to stay with a baseline-like season length of about 170 days and 10 seasons.

Our results for “LSST + follow-up” suggests little reason to extend the WFD by  $6700 \text{ deg}^2$  (compare “kraken\_2044” and “colossus\_2667”, and “Pontus\_2002” and “baseline2018a”) and for “LSST only” strategies with a smaller WFD footprint perform even better. Therefore we suggest to stick with the WFD footprint of  $18000 \text{ deg}^2$  but we are also fine with  $24700 \text{ deg}^2$ . More important than constraints on the area is the replacement of the  $2 \times 15 \text{ s}$  exposure by  $1 \times 30 \text{ s}$  to improve efficiency (compare “kraken\_2042” to “baseline2018a”). Another interesting scenario to investigate is the redistribution from visits in  $y$  band to more useful bands for LSNe Ia as done in “alt\_sched”. This means going from a distribution of visits in  $ugrizy$ : (6.8, 9.4, 21.5, 21.6, 20.2, 20.4)% to (8.2, 11.0, 27.6, 18.1, 25.6, 9.5)%. Because of the many differences between “alt\_sched” and “baseline2018a”, a direct comparison is impossible but we expect some improvement. To quantify this, a simulation implementing the redistribution with the greedy algorithm used for “baseline2018a” would be helpful.

Further, a very important result: most rolling cadence strategies are disfavored for our LSNe Ia science case. For these cadence strategies, the shortened cumulative season lengths  $\bar{t}_{\text{eff,cad}}$  lead to an overall more negative impact on the number of LSNe Ia with delays, compared to the gain from the increased sampling frequency.

#### 6.4. Different follow-up scenarios

In this section, the prospects of increasing the number of LSNe Ia by assuming different follow-up scenarios are discussed. For this purpose, we have investigated a sample of 100 mock LSNe Ia (50 mock quads and 50 mock doubles). The result for the standard follow-up case is shown in Table 5 first row for the two cadence strategies “baseline2018a” and “alt\_sched”. To clarify, the standard follow-up scenario assumes observations in the 3 filters  $g$ ,  $r$  and  $i$ , going to a depth of  $m_{5,g} = 24.60 \text{ mag}$ ,  $m_{5,r} = 24.23 \text{ mag}$  and  $m_{5,i} = 23.67 \text{ mag}$ . Follow-up is assumed every second night in all 3 filters two days after the third data point exceeds the  $5\sigma$  depth in any filter.

An alternative follow-up scenario would be to observe in bands  $r$ ,  $i$  and  $z$ . The numbers in the second row are slightly worse than those for following up in bands  $g$ ,  $r$  and  $i$  and therefore this scenario is to be rejected.

The more aggressive approach is to trigger follow-up after the second data point exceeds the  $5\sigma$  depth (see row 3). The improvement of 10 to 27% might look promising, but also many more false positives will be detected and therefore some observing time would likely be wasted on false positives.

Of further interest is also the cadence of the follow-up observation. Therefore we consider two additional cases where we follow-up daily (see row 4) and every third day (see row 5), in-

	row	baseline2018a	alt_sched
LSST + follow-up	1	16.5 (22.4%)	21.0 (33.9%)
follow-up in bands $riz$	2	15.0 (20.4%)	20.2 (32.7%)
follow-up after 2 data points	3	21.0 (28.6%)	23.0 (37.3%)
daily follow-up	4	19.4 (26.4%)	23.3 (37.8%)
follow-up every third day	5	13.5 (18.4%)	18.0 (29.2%)
deeper follow-up (1 mag)	6	28.2 (38.4%)	27.0 (43.8%)
deeper follow-up (2 mag)	7	37.1 (50.6%)	34.0 (55.0%)
deeper follow-up (4 mag)	8	39.4 (53.7%)	37.6 (60.9%)
no microlensing	9	35.7 (48.6%)	33.3 (53.9%)
no microl., 1 mag deeper	10	48.4 (65.9%)	43.2 (69.9%)

Table 5: This table summarizes the investigation of different follow-up strategies and shows, in addition, the prospects of an improved analysis technique concerning the modeling of microlensing. For the two strategies “baseline2018a” and “alt\_sched”, the number of LSNe Ia with good time delays over the 10-year survey are shown for each considered scenario. The percentages in the brackets show how many of the total numbers of LSNe Ia have good time delays. For this purpose 100 mock LSNe Ia have been investigated. The exact definition of “LSST + follow-up” (row 1) is described in the text and the scenarios from rows 2 to 8 are alternative follow-up scenarios detailed in the text. Rows 9 and 10 are hypothetical numbers interesting for future improved analysis techniques of microlensing.

stead of the standard follow-up of every second day. While going down to observations every three days decreases the number of LSNe Ia with good delays by about 18%, daily visits improve on a level of 11 to 18%. Going from a two-days to a single day cadence increases the effort of follow-up significantly by increasing the numbers of LSNe Ia only slightly.

A more promising approach is to keep the follow-up observations every two days but increase the depth. To go one magnitude deeper (see row 6) than the average baseline depth a total observing time of  $\sim 45 \text{ min}$  per night is needed for a 2 m telescope as in Section 6.3, which is feasible. For “alt\_sched”, this leads to an improvement of 29% in comparison to the standard follow-up scenario and therefore slightly better than the daily follow-up case. For “baseline2018a”, the improvement is 71% and therefore definitely worth considering the effort (compare upper two panels in Figure 15).

Another possibility is to go 2 magnitudes deeper but therefore we have to observe  $\sim 2 \text{ h}$  per night to get observations in 3 filters. This seems only feasible for a 2-meter-telescope which can observe simultaneously in 3 filters or by a telescope with a larger diameter. For “alt\_sched”, this means an improvement in comparison to the standard follow-up scenario of 62% and for “baseline2018a” an improvement of 125%. Going another 2 magnitudes deeper does not increase the number of LSNe Ia significantly and therefore going beyond 2 magnitudes is definitely not worth the effort (compare rows 7 and 8 in Table 5).

A limiting factor of our analysis is the microlensing effect which is not taken into account in our time-delay measurement with PyCS and therefore we are not able to accurately measure short time delays (see Figure 12 and the upper two panels of Figure 15) because we do not model the bias due to microlensing magnification, which is an absolute bias in time, whereas the accuracy is relative to the length of the delay. In rows 9 and 10 of Table 5, we see that we could increase the number of LSNe Ia with good delays by a factor of 60% to 120% in the best case scenario, where we imagine a perfect correction for microlensing deviations. This would give us access to short time-delays

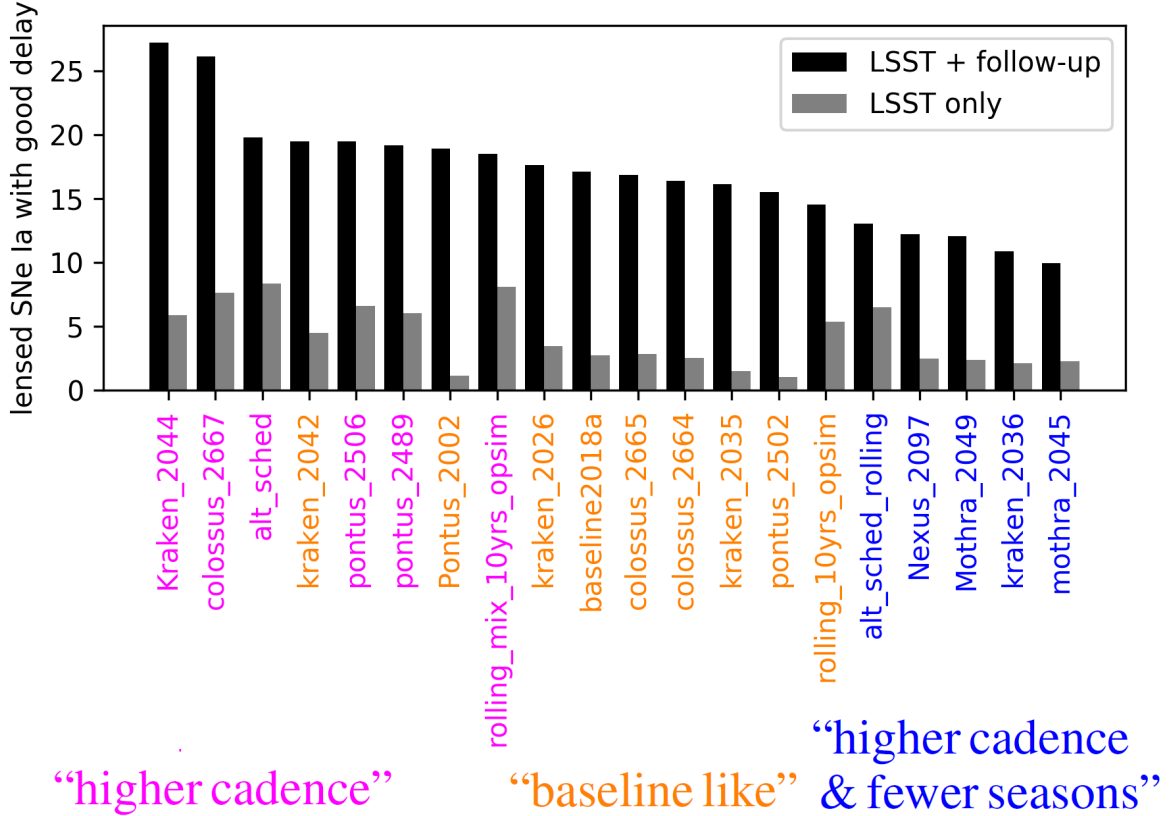


Fig. 14: The number of LSNe Ia for the 10-year survey where the time delay has been measured with accuracy  $< 1\%$  and precision  $< 5\%$  by using LSST as a discovery machine in combination with follow-up observations for measuring time delays (black bars) and using only LSST data (grey bars, see also Figure 11). Follow-up is every second night in filters  $g$ ,  $r$  and  $i$ , starting two nights after third LSST detection (with brightness exceeding  $5\sigma$  depth in any filter). With follow-up observations, we get a substantial increase in the number of LSNe Ia systems with good measured delays.

as visible in the comparison of the upper two panels and the lower two panels of Figure 15 and therefore encourages the use of color curves instead of light curves to reduce the impact of microlensing on the delay measurement as suggested by Goldstein et al. (2018b) and discussed in Appendix A. Also, the approach of using SNe Ia templates to fit the intrinsic light curve shape including effects of microlensing might be reasonable and produce higher fraction of good delays. Some of these are currently being explored (Pierel & Rodney 2019; Collett et al., in prep, T. Collett, priv. comm.).

## 7. Discussion and summary

In this work, we explored different LSST cadence strategies for measuring time delays in strongly lensed SNe Ia. As illustrated in Figure 14, we have found that using LSST just as discovery machine in combination with high cadence follow-up observation for the delay measurement is the best way to increase the number of LSNe Ia with good time delays. In contrast, using only LSST data is not ideal.

To estimate the resulting  $H_0$  constraint from a sample of LSST LSNe Ia, we assume that each LSNe Ia system with good delays yields typically an  $H_0$  measurement with  $\sim 5\%$  uncertainty in flat  $\Lambda$ CDM (including all sources of uncertainties such as the time-delay uncertainty investigated in this paper, and lens mass modeling uncertainties). This is currently achieved with the best lensed quasar systems of the HOLiCOW sample, and serves as a reference given that we expect LSNe Ia to yield

similar or better constraints than that of lensed quasars. While focussing only on LSNe Ia with good delays could potentially introduce selection bias, we suspect such biases to be small and, if present, could be corrected (e.g., Collett & Cunningham 2016). Thus, for a sample of  $N$  lenses, the uncertainty on  $H_0$  would scale approximately as  $\sim 5\%/\sqrt{N}$ , assuming Gaussian uncertainties. With LSST data only, the number of lensed SNe Ia from our investigation (Figure 14) ranges from  $\sim 1$  to  $\sim 8$ , depending on the strategy. This would yield an  $H_0$  constraint with  $\sim 2 - 5\%$  uncertainty from the sample. In the case of LSST with follow-up, the number of lensed SNe increase substantially, varying from  $\sim 10$  to  $\sim 28$ , translating to an  $H_0$  constraint with  $\sim 1 - 2\%$  uncertainty. Therefore, with optimal LSST observing strategy and fast-response follow-up, we would reach percent-level constraint on  $H_0$ , which is a factor of 2 to 5 lower in uncertainty compared to the case of LSST-only scenario.

From the investigated cadence strategies for the follow-up scenario, we have found that observing strategies with an improved sampling by keeping everything else baseline-like is, in general, the best observing strategy for our science case. An ideal strategy is presented in the following key points:

- 10 seasons with a season length of 170 days or longer
- WFD footprint of  $18\,000\text{ deg}^2$  up to  $24\,700\text{ deg}^2$
- One revisit within a night in a different filter than the first visit
- Replacement of  $2 \times 15\text{ s}$  exposure by  $1 \times 30\text{ s}$

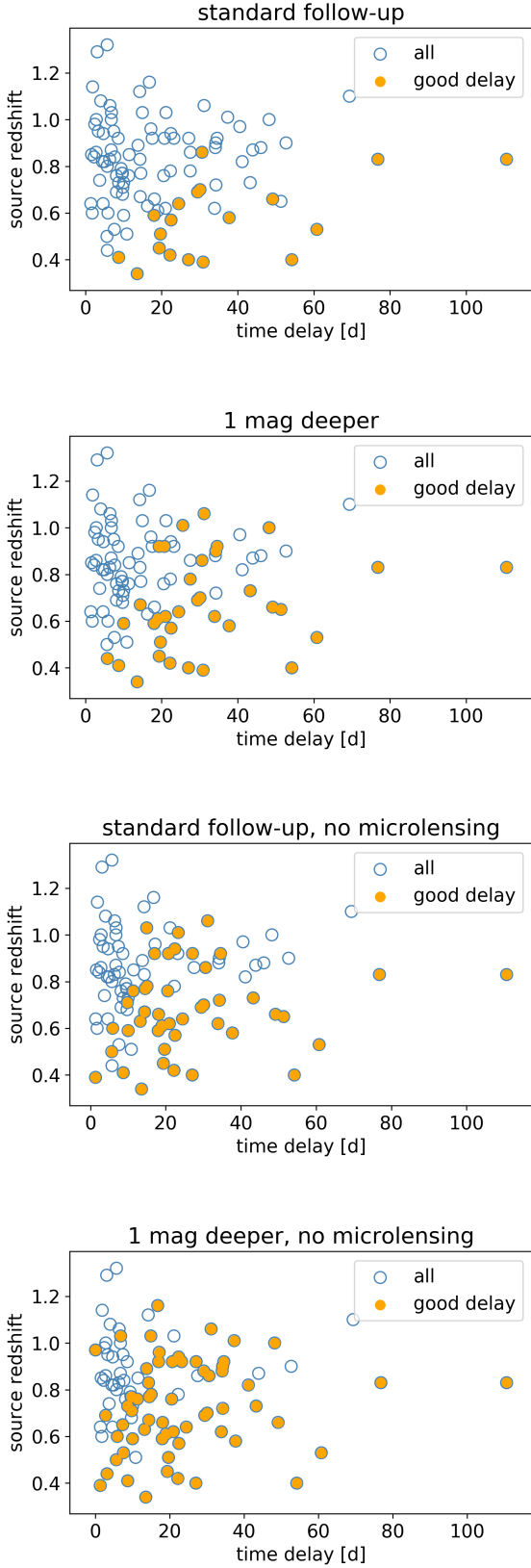


Fig. 15: Time-delay and source-redshift distribution for 100 investigated mock LSNe for “baseline2018a”, similar to Figure 12. The upper two panels show the standard follow-up observation (first panel) and the option going 1 magnitude deeper (second panel). The lower two panels show the same follow-up scenarios hypothetically without microlensing. The distributions vary slightly because for a quad system just a single time delay is shown, either the first successfully measured delay or the maximum of the 6 possible delays.

– Distribution of visits like “alt\_sched” [*ugrizy* as  $\sim$  (8.2, 11.0, 27.6, 18.1, 25.6, 9.5)%].

Another very important point is that most of the suggested rolling cadences are clearly disfavored for our science case because many LSNe Ia will not even be detected due to the reduced cumulative season length. The only rolling cadence which performed well is `rolling_mix_10yrs_opsim`, but this is most likely because the WFD stays on in the background and additionally revisits are done in different filters, which can partly compensate for the not ideal “rolling” feature.

We have assumed that follow-up observations starts two days after the third LSST data point exceeds the  $5\sigma$  depth. The follow up is done every second night in 3 filters *g*, *r* and *i* to a depth of  $m_{5,g} = 24.60$  mag,  $m_{5,r} = 24.23$  mag and  $m_{5,i} = 23.67$  mag, which is feasible with a 2-meter telescope. To improve on that mainly a greater depth is of interest. Follow-up observations going 1 magnitude deeper than the baseline  $5\sigma$  depth, or even 2 magnitude deeper, if feasible, will increase the number of LSNe Ia with good time-delays significantly. Going beyond 2 magnitude deeper is not worth the effort.

We would like to point out that we have only investigated LSNe Ia. Although a single lensed Core-Collapse (CC) SN is less valuable than a LSNe Ia (given the standardizable light curves of SNe Ia), the larger sample of CC SNe which will be detected by LSST makes them as well relevant for time-delay cosmography. Due to the different light curve shapes and luminosities the optimal cadence strategy for measuring time delays in CC SNe might be different from the one for LSNe Ia. At least in terms of total number of lensed CC SNe the strategies will be ordered in the same way as in Table 2 but the numbers will be a factor of 1.8 higher (Oguri & Marshall 2010). In terms of measuring time delays the improved sampling requested from our investigation of LSNe Ia will be also helpful for the case of CC SNe. To investigate the prospects of measuring time delays in lensed CC SNe similar to the case of LSNe Ia the specific intensity from a theoretical model is required.

In terms of analyzing the data it seems promising to find ways to reduce the impact of microlensing. One possibility will be the use of color curves instead of light curves. To do this, it might be worth to implement SNe template fitting instead of splines into PyCS. With the recent discovery of the very first LSNe system and the expected sample from LSST, our work demonstrates that time-delay cosmography as envisioned by Refsdal (1964) has bright prospects in the LSST era.

*Acknowledgements.* We thank W. Hillebrandt, S. Blondin, D. A. Goldstein for useful discussions, and the internal LSST DESC reviewers S. Rodney, A. Goobar, and T. E. Collett for their feedback that improved the presentation of our paper. SH and SHS thank the Max Planck Society for support through the Max Planck Research Group for SHS. This project has received funding from the European Research Council (ERC) under the European Union’s Horizon 2020 research and innovation programme (grant agreement No 771776). This research was supported in part by Perimeter Institute for Theoretical Physics. Research at Perimeter Institute is supported by the Government of Canada through the Department of Innovation, Science and Economic Development and by the Province of Ontario through the Ministry of Research, Innovation and Science. UMN has been supported by the Transregional Collaborative Research Center TRR33 ‘The Dark Universe’ of the Deutsche Forschungsgemeinschaft. VB, JHHC and FC acknowledge support from the Swiss National Science Foundation and through European Research Council (ERC) under the European Union’s Horizon 2020 research and innovation programme (COSMICLENS: grant agreement No 787866). DR acknowledges support from the National Science Foundation Graduate Research Fellowship under Grant No. DGE 1752814. HA has been supported by the Rutgers Discovery Informatics Institute Fellowship of Excellence in Computational and Data Science for academic years 2017-2018, 2018-2019. MK acknowledges support from the Klaus Tschira Foundation. This work was supported in part by World Premier International Research Center Initiative (WPI Initiative), MEXT, Japan, and JSPS KAKENHI

Grant Number JP15H05892 and JP18K03693. The DESC acknowledges ongoing support from the Institut National de Physique Nucléaire et de Physique des Particules in France; the Science & Technology Facilities Council in the United Kingdom; and the Department of Energy, the National Science Foundation, and the LSST Corporation in the United States. DESC uses resources of the IN2P3 Computing Center (CC-IN2P3–Lyon/Villeurbanne - France) funded by the Centre National de la Recherche Scientifique; the National Energy Research Scientific Computing Center, a DOE Office of Science User Facility supported by the Office of Science of the U.S. Department of Energy under Contract No. DE-AC02-05CH11231; STFC DiRAC HPC Facilities, funded by UK BIS National E-infrastructure capital grants; and the UK particle physics grid, supported by the GridPP Collaboration. This work was performed in part under DOE Contract DE-AC02-76SF00515.

## References

- Barnabè, M., Czoske, O., Koopmans, L. V. E., Treu, T., & Bolton, A. S. 2011, *MNRAS*, 415, 2215
- Bessell, M. & Murphy, S. 2012, *PASP*, 124, 140
- Birrer, S. et al. 2018
- Bonvin, V., Tewes, M., Courbin, F., et al. 2016, *A&A*, 585, A88
- Bonvin, V., Tihhonova, O., Millon, M., et al. 2018, arXiv e-prints
- Bonvin, V. et al. 2018, *A&A*, 616, A183
- Collett, T. E. & Cunningham, S. D. 2016, *MNRAS*, 462, 3255
- Courbin, F., Bonvin, V., Buckley-Geer, E., et al. 2017, ArXiv e-prints
- Dobler, G. & Keeton, C. R. 2006, *ApJ*, 653, 1391
- Eigenbrod, A., Courbin, F., Vuissoz, C., et al. 2005, *A&A*, 436, 25
- Falco, E. E., Gorenstein, M. V., & Shapiro, I. I. 1985, *ApJ*, 289, L1
- Foxley-Marrable, M., Collett, T. E., Vernardos, G., Goldstein, D. A., & Bacon, D. 2018, *MNRAS*, 478, 5081
- Goldstein, D. A. & Nugent, P. E. 2017, *ApJ*, 834, L5
- Goldstein, D. A., Nugent, P. E., & Goobar, A. 2018a
- Goldstein, D. A., Nugent, P. E., Kasen, D. N., & Collett, T. E. 2018b, *ApJ*, 855, 22
- Goobar, A. et al. 2017, *Science*, 356, 291
- Grillo, C. et al. 2018, *ApJ*, 860, 94
- Jee, I., Komatsu, E., Suyu, S. H., & Huterer, D. 2016, *J. Cosmology Astropart. Phys.*, 4, 031
- Jones, E., Oliphant, T., Peterson, P., et al. 2001, *SciPy: Open source scientific tools for Python*, [Online; accessed *today*]
- Kasen, D., Thomas, R. C., & Nugent, P. 2006, *ApJ*, 651, 366
- Kayser, R., Refsdal, S., & Stabell, R. 1986, *A&A*, 166, 36
- Kelly, P. L. et al. 2016a, *ApJ*, 819, L8
- Kelly, P. L. et al. 2016b, *ApJ*, 831, 205
- Kormann, R., Schneider, P., & Bartelmann, M. 1994, *A&A*, 284, 285
- Kromer, M. & Sim, 2009, *MNRAS*, 398, 1809
- Linder, E. V. 2011, *Phys. Rev. D*, 84, 123529
- Lochner, M., Scolnic, D. M., Awan, H., et al. 2018, arXiv e-prints
- LSST Science Collaboration. 2009, ArXiv e-prints
- Lucy, L. B. 1999, *A&A*, 344, 282
- Lucy, L. B. 2002, *A&A*, 384, 725
- Lucy, L. B. 2003, *A&A*, 403, 261
- Lucy, L. B. 2005, *A&A*, 429, 19
- Marshall, P. et al. 2017
- Mihalas, D. & Weibel-Mihalas, B. 1999, *Foundations of Radiation Hydrodynamics*, Dover Books on Physics (Dover Publications)
- Molinari, N., Durand, J.-F., & Sabatier, R. 2004, *Computational Statistics & Data Analysis*, 45, 159
- More, A., Suyu, S. H., Oguri, M., More, S., & Lee, C.-H. 2017, *ApJ*, 835, L25
- Nomoto, K., Thielemann, F.-K., & Yokoi, K. 1984, *ApJ*, 286, 644
- Oguri, M. 2010, *PASJ*, 62, 1017
- Oguri, M., Inada, N., Strauss, M. A., et al. 2012, *AJ*, 143, 120
- Oguri, M. & Marshall, P. J. 2010, *MNRAS*, 405, 2579
- Pakmor, R., Hachinger, S., Röpke, F. K., & Hillebrandt, W. 2011, *A&A*, 528, A117
- Pakmor, R., Kromer, M., Taubenberger, S., et al. 2012, *ApJ*, 747, L10
- Pierel, J. R. & Rodney, S. A. 2019, arXiv e-prints (1902.01260)
- Planck Collaboration. 2018
- Quimby, R. M., Oguri, M., More, A., et al. 2014, *Science*, 344, 396
- Refsdal, S. 1964, *MNRAS*, 128, 307
- Riess, A. G. et al. 2016, *ApJ*, 826, 56
- Riess, A. G. et al. 2018, *ApJ*, 861, 126
- Rodney, S. A. et al. 2016, *ApJ*, 820, 50
- Roepke, F. K. 2005, *A&A*, 432, 969
- Schneider, P. & Sluse, D. 2014, *A&A*, 564, A103
- Seitzzahl, I. R., Ciaraldi-Schoolmann, F., Röpke, F. K., et al. 2013, *MNRAS*, 429, 1156

- Shajib, A. J., Treu, T., & Agnello, A. 2018a, *MNRAS*, 473, 210
- Shajib, A. J., Treu, T., & Agnello, A. 2018b, *MNRAS*, 473, 210
- Sim, S. A., Röpke, F. K., Hillebrandt, W., et al. 2010, *ApJ*, 714, L52
- Suyu, S. H., Chang, T.-C., Courbin, F., & Okumura, T. 2018, *Space Science Reviews*, 214, 91
- Suyu, S. H. et al. 2017, *MNRAS*, 468, 2590
- Tewes, M., Courbin, F., & Meylan, G. 2013, *A&A*, 553, A120
- Vernardos, G. & Fluke, C. J. 2013, *MNRAS*, 434, 832
- Vernardos, G., Fluke, C. J., Bate, N. F., Croton, D., & Vohl, D. 2015, *ApJ Suppl.*, 217, 23
- Wambsganss, J., Witt, H. J., & Schneider, P. 1992, *A&A*, 258, 591
- Yahalom, D. A., Schechter, P. L., & Wambsganss, J. 2017
- Yildırım, A., van den Bosch, R. C. E., van de Ven, G., et al. 2017, *MNRAS*, 468, 4216

## Appendix A: Case study of microlensing on LSNe Ia

To illustrate the effect of microlensing on LSNe Ia in detail we calculate microlensed spectra and light curves. For this we assume an iPTF16geu-like (Goobar et al. 2017) configuration, which means the source redshift  $z_S = 0.409$  and the lens redshift  $z_L = 0.216$ . The redshifts are needed to calculate the size of a pixel  $\Delta d_{\text{mag}} = 1.12 \times 10^{13} \text{ cm} = 3.62 \times 10^{-6} \text{ pc}$  of the magnification map which corresponds to an angular scale of  $\Delta d_{\text{mag}}/D_s = 3.28 \times 10^{-15} \text{ rad} = 6.76 \times 10^{-10} \text{ arcsec}$ . Since we only determine absolute magnitudes and rest-frame fluxes in this section, we set  $z = 0$  and  $D_L = D_A = 10 \text{ pc}$  in Equations (13)<sup>18</sup> and (14).

For this case study, we look at two specific example realizations where we place a SNe Ia in two different positions of the magnification map from Figure 1, corresponding to image A of iPTF16geu (More et al. 2017).

First we consider the position  $(x, y) = (12000, 8600)$  and compare the non-microlensed flux  $F_{\lambda_j, \text{cart}, \mu=1}(t_i)$  with the microlensed one  $F_{\lambda_j, \text{cart}}(t_i)$  for two different instances in time as illustrated in Figure A.1. Panels a) to d) correspond to  $t = 14.9 \text{ d}$  and e) to h) to  $t = 39.8 \text{ d}$ . For both times, the zoomed-in magnification map (panels a and e) from Figure 1 is provided, with the position and radius of the SN shown by a cyan circle. The radius is defined via the area of the SN, which contains 99.9% of the total projected specific intensity  $\sum_{j,l,m} I_{\lambda_j, e}(t_i, x_l, y_m)$ . In addition, the normalized specific intensity profiles (panels b and f) are shown, where the vertical blue line corresponds to the radius of the SN and the dashed black line marks the distance between the center of the SN and the caustic in the magnification map which separates low and high magnification regions. The normalized specific intensity of filter band X is defined as

$$I_{X, \text{norm}} = \frac{I_X}{\max(I_X)}, \quad (\text{A.1})$$

which corresponds to a radial radiation distribution for a given filter X. Furthermore the fluxes for the cases with microlensing and without (panels c and g) are shown together with their relative strength (panels d and h).

For  $t = 14.9 \text{ d}$ , the SN is completely in a homogeneous region of demagnification as shown in panel a) of Figure A.1 and therefore the flux is demagnified by the same amount for all wavelengths, as can be seen in panel c) and more clearly in panel d)<sup>19</sup> independent of the specific intensity profiles. For the later time,  $t = 39.8 \text{ d}$ , the SN has expanded further and crosses

<sup>18</sup>  $\Delta d_{\text{mag}} = 1.12 \times 10^{13} \text{ cm}$  or the interpolated value to fulfill Equation (12) is used for  $\Delta x_l$  and  $\Delta y_m$ .

<sup>19</sup> Note the scale difference between panels d) and h) is a factor of 600.

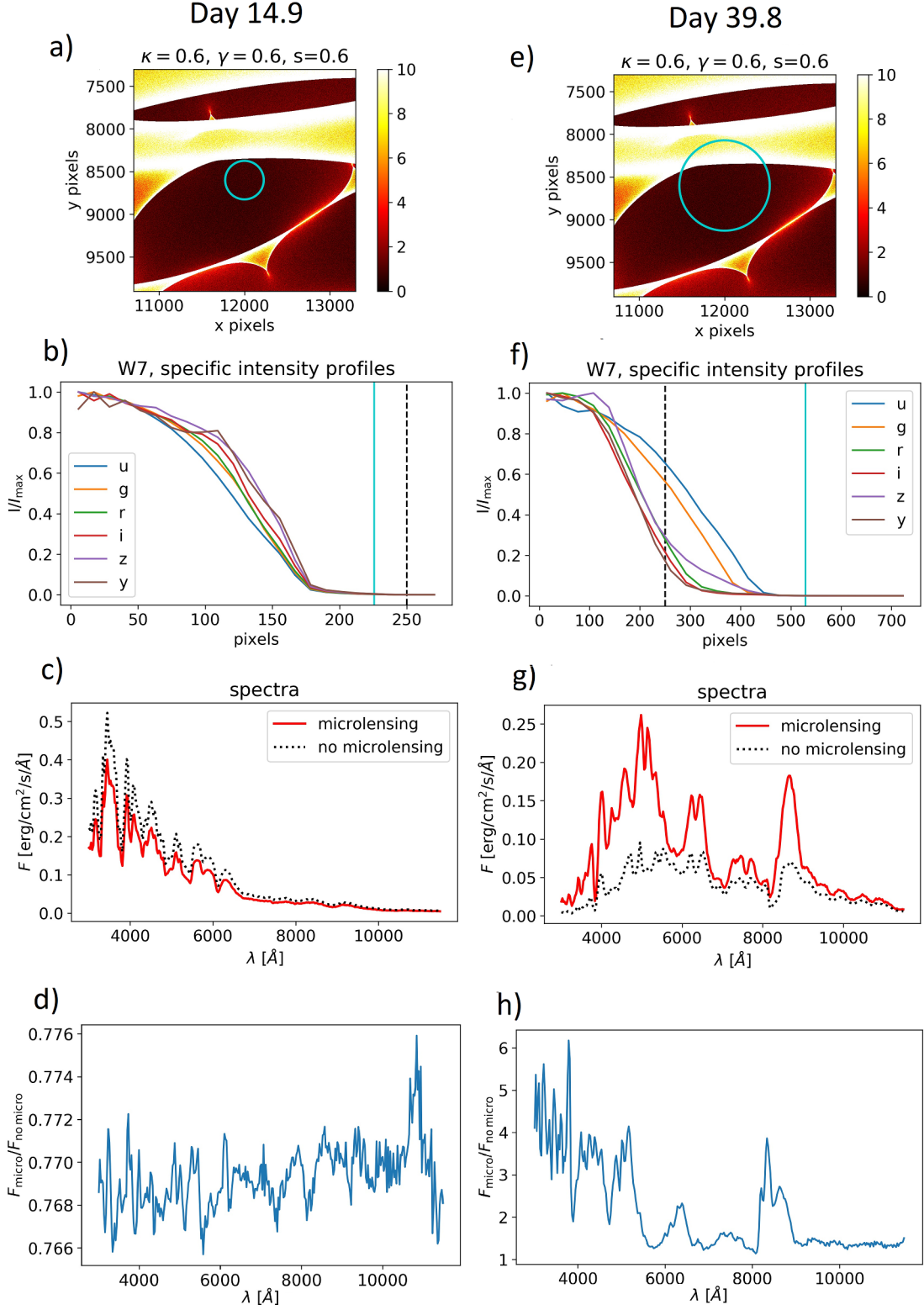


Fig. A.1: These plots show the effect of microlensing on a rest-frame spectrum of a SN Ia centered at pixels  $(x, y) = (12000, 8600)$  in the microlensing map from Figure 1 for two different rest-frame times since explosion  $t$ . The size of one pixel as defined in Equation 3 is  $\Delta d_{\text{mag}} = 3.62 \times 10^{-6}$  pc. For a better understanding of the microlensing effect, the microlensing map (panels a and e), the intensity profiles (panels b and f), the spectra (panels c and g) and the ratio (panels d and h) between the microlensed and non-microlensed spectra are shown. On the microlensing map, the radius of the SN is shown in cyan. This radius is defined via the area of the SN which contains 99.9% of the total specific intensity  $\sum_{j,l,m} I_{\lambda,j,e}(t_i, x_l, y_m)$ . The vertical dashed black line in the intensity profiles shows the distance from the center of the SN to the caustic of the microlensing map, which separates the regions of high and low magnification. The vertical cyan line indicates the SN radius. The spectra show the case of microlensing and no microlensing, where the ratio of those two is shown in the plot below the spectra. Apart from an overall demagnification for  $t = 14.9$  d, the microlensing has no significant influence on the spectrum. However, for the case of  $t = 39.8$  d, there is a significant difference between the bluer and redder part of the spectrum. The influence on the two light curves,  $u$  and  $r$ , and the corresponding color curve is shown in Figure A.2.

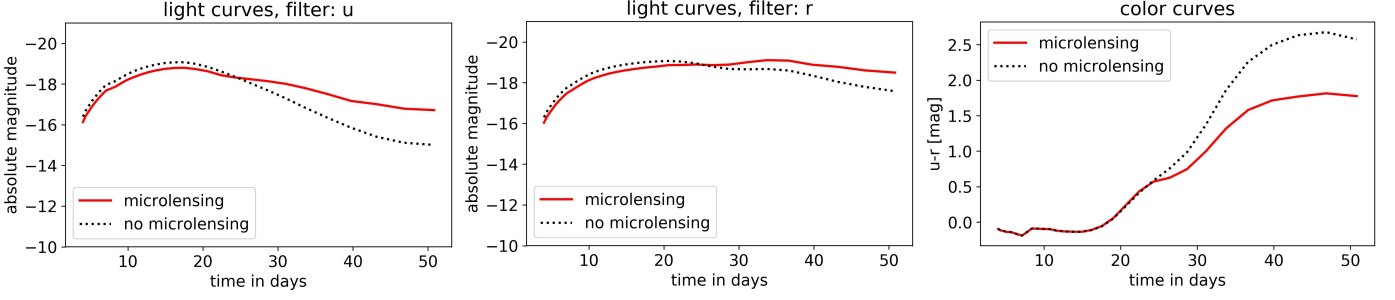


Fig. A.2: Influence of microlensing on two light curves and the corresponding color curve for the SN shown in Figure A.1. As long as the demagnification due to microlensing is similar in  $u$  and  $r$  bands, it cancels out in the color curve.

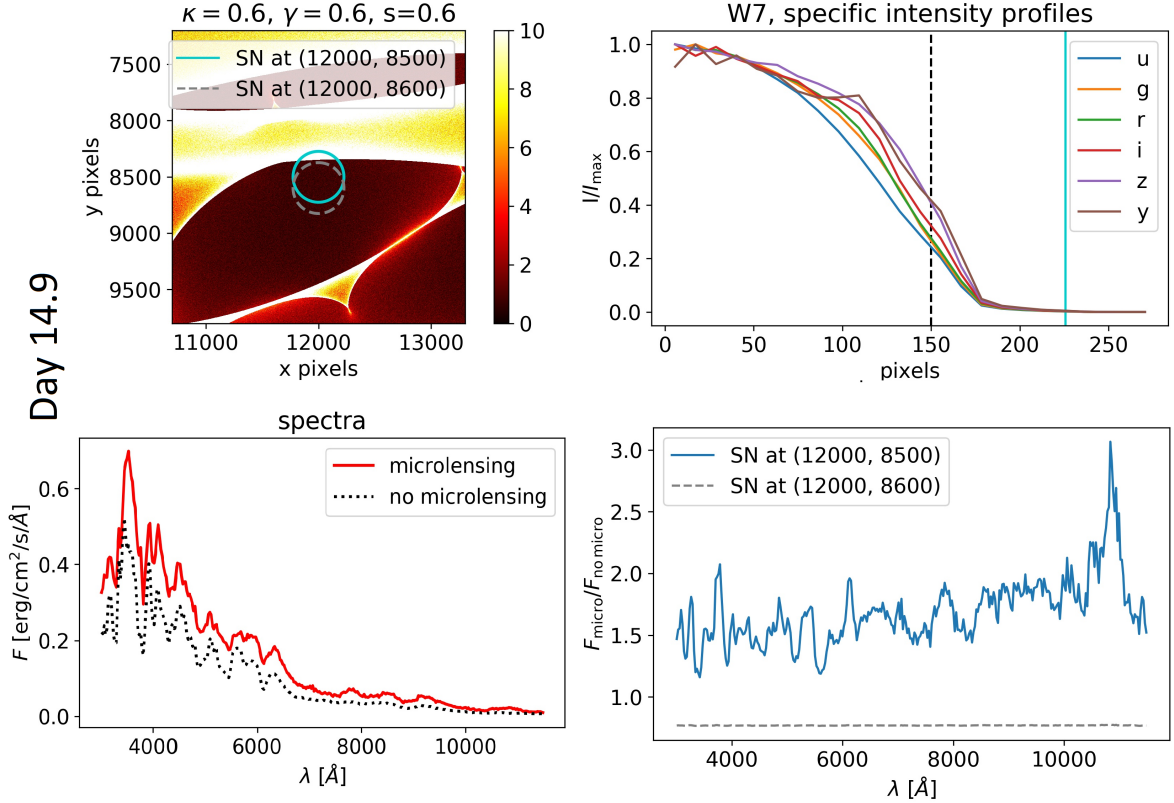


Fig. A.3: These plots show the effect of microlensing on a SN Ia spectrum at rest-frame time  $t = 14.9$  d after explosion, similar as in Figure A.1 but at a slightly different position of the SN:  $(x, y) = (12000, 8500)$ . For a better comparison, the case from Figure A.1 is shown as gray dashed line in the upper-left and lower-right panels. The size of one pixel as defined in Equation 3 is  $\Delta d_{\text{mag}} = 3.62 \times 10^{-6}$  pc. Although the specific intensity profiles are similar for different filters, microlensing is clearly visible in the flux ratio.

over a caustic as visible in panel e), such that the outer region of the SN is partly in a region of high magnification. From the specific intensity profiles in panel f) we see that the outer ejecta region emits stronger in the bluer bands ( $u$  and  $g$ ) than in the red ones ( $r$ ,  $i$ ,  $z$  and  $y$ ). This explains the overall trend that the blue part of the spectrum is more magnified than the red part, which is indeed seen in panels g) and h).

For the case constructed in Figure A.1 we see a significant impact on the light curves due to microlensing as shown in red in Figure A.2 where the light curves are highly distorted. For the  $u$ - $r$  color curve, the effect of microlensing cancels out up to day 25. Afterwards the crossing of the micro caustics, separating regions of low and high magnification, in combination with

different spatial distributions of the radiation in  $u$  and  $r$  band becomes important. This is an example for the so-called *achromatic phase* as reported by Goldstein et al. (2018b), who find that color curves up to day 20 after explosion are nearly independent of microlensing. They claim this is due to the similar specific intensity profiles for early days and more different ones at later days, as we can also see for our case comparing panel b) and f) in Figure A.1.

For further investigation we construct another test case where the caustic of the magnification map will be crossed during the achromatic phase, as shown in Figure A.3. Here the microlensing effect is clearly visible in the flux ratio, although the specific intensity profiles are more similar as for later days (com-

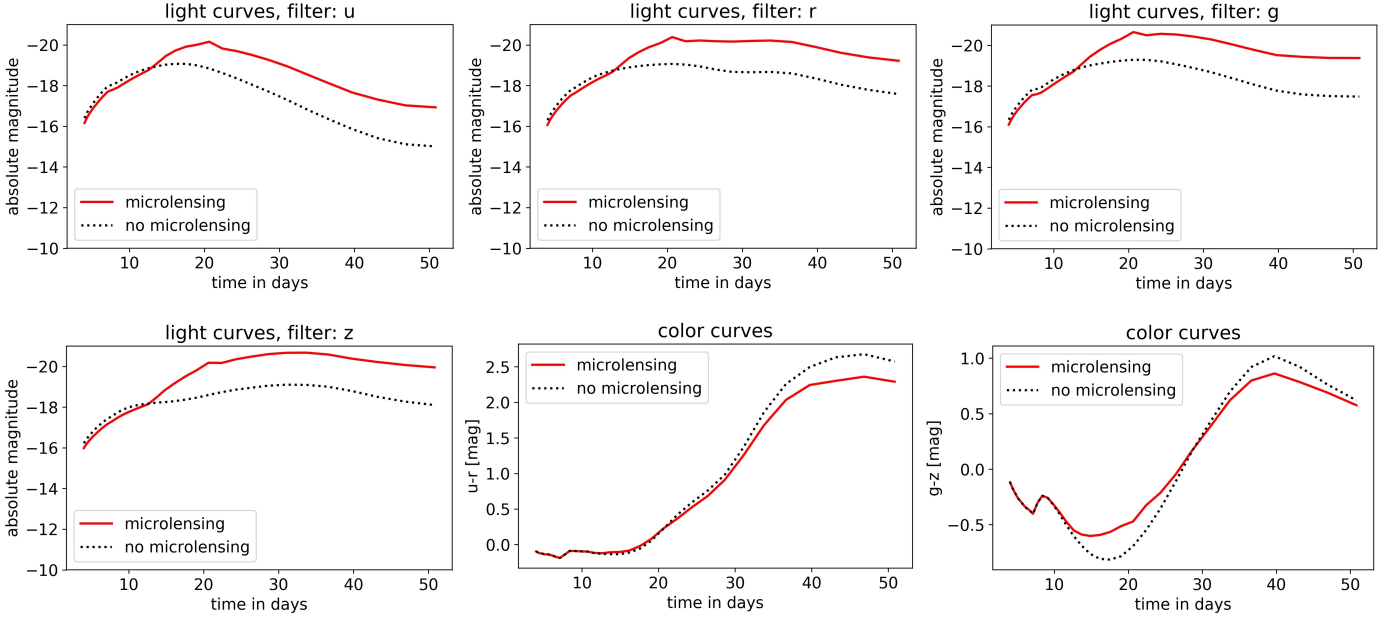


Fig. A.4: Influence of microlensing on light curves and color curves for the SN shown in Figure A.3. Whereas the light curves are highly influenced by microlensing, the color curve  $u-r$  is very similar for the case of microlensing and non-microlensing. This is not the case for all color curves, as shown for example by  $g-z$ .

pare panels b and f of Figure A.1). Also, the influence on the light curves is visible earlier and more drastic as shown in Figure A.4. The light curves are highly distorted and peaks are shifted, which adds large uncertainty to the time-delay measurement between different images based on light curves that undergo different microlensing. Even though the  $u-r$  color curve compensates microlensing in early phases quite well and is therefore promising for measuring time delays, this is not true for all color curves as shown for the case of  $g-z$ . Here, the microlensed and non-microlensed curves deviate from each other even though they are in the achromatic phase.

To explore this further, we consider a large sample of 10000 random SN positions in the magnification map shown in Figure 1. For each position, we calculate the light curves using Equation (15) and then calculate the color curves. For each time bin  $t_i$ , we calculate from the sample the 50th percentile as well as the  $1-\sigma$  and  $2-\sigma$  spread. The results for all rest-frame LSST color curves are shown in Figures A.5 and A.6, where the vertical black line marks the time when the  $2-\sigma$  spread is the first time beyond 0.1mag. We find the general trend that the achromatic phase in the color curves becomes shorter the further the different bands are apart. As in Goldstein et al. (2018b), we find an achromatic phase-like behavior until 25 to 30 days after explosion, but only for rest-frame color curves containing combinations of  $u$ ,  $g$ ,  $r$  or  $i$  bands (except  $u-i$ ) or the color curve  $z-y$  (Figure A.5). As soon as we combine one of the bands  $u$ ,  $g$ ,  $r$  or  $i$  with  $z$  or  $y$  we see the influence of microlensing earlier (Figure A.6). This behavior can be explained by looking at the normalized specific intensity profiles for early times as shown in panel b) of Figure A.1: The profiles for the outer region (pixel 150 to 200) are similar for filters  $z$  and  $y$ , but different from  $u$ ,  $g$ ,  $r$  and  $i$ . Since the achromatic phase depends highly on the specific intensity profiles, the investigation of different explosion models is necessary to explore this further (S. Huber et al., in preparation).

In addition to the different durations of the achromatic phase for the various color curves, we note that some of our

color curves from ARTIS are different in shape from those of SEDONA in Goldstein et al. (2018b). It is also very important to emphasize that our results in this section are for rest-frame color curves, which means that different color curves will be more or less useful depending on the redshift of the source.

## Appendix B: Photometric uncertainty of LSST

The photometric uncertainty  $\sigma_1$  from Equation 17 is defined as:

$$\sigma_1^2 = \sigma_{\text{sys}}^2 + \sigma_{\text{rand}}^2, \quad (\text{B.1})$$

where  $\sigma_{\text{sys}} = 0.05$  and

$$\sigma_{\text{rand}}^2 = (0.04 - \gamma^c)x + \gamma^c x^2 (\text{mag}^2). \quad (\text{B.2})$$

$\gamma^c$  varies from 0.037 to 0.040 for different filters and  $x = 10^{4(m-m_5)}$ , where  $m$  is the magnitude of the SN data point and  $m_5$  is the  $5\sigma$  point-source depth (for more details see LSST Science Collaboration (2009), Sec. 3.5, p. 67).

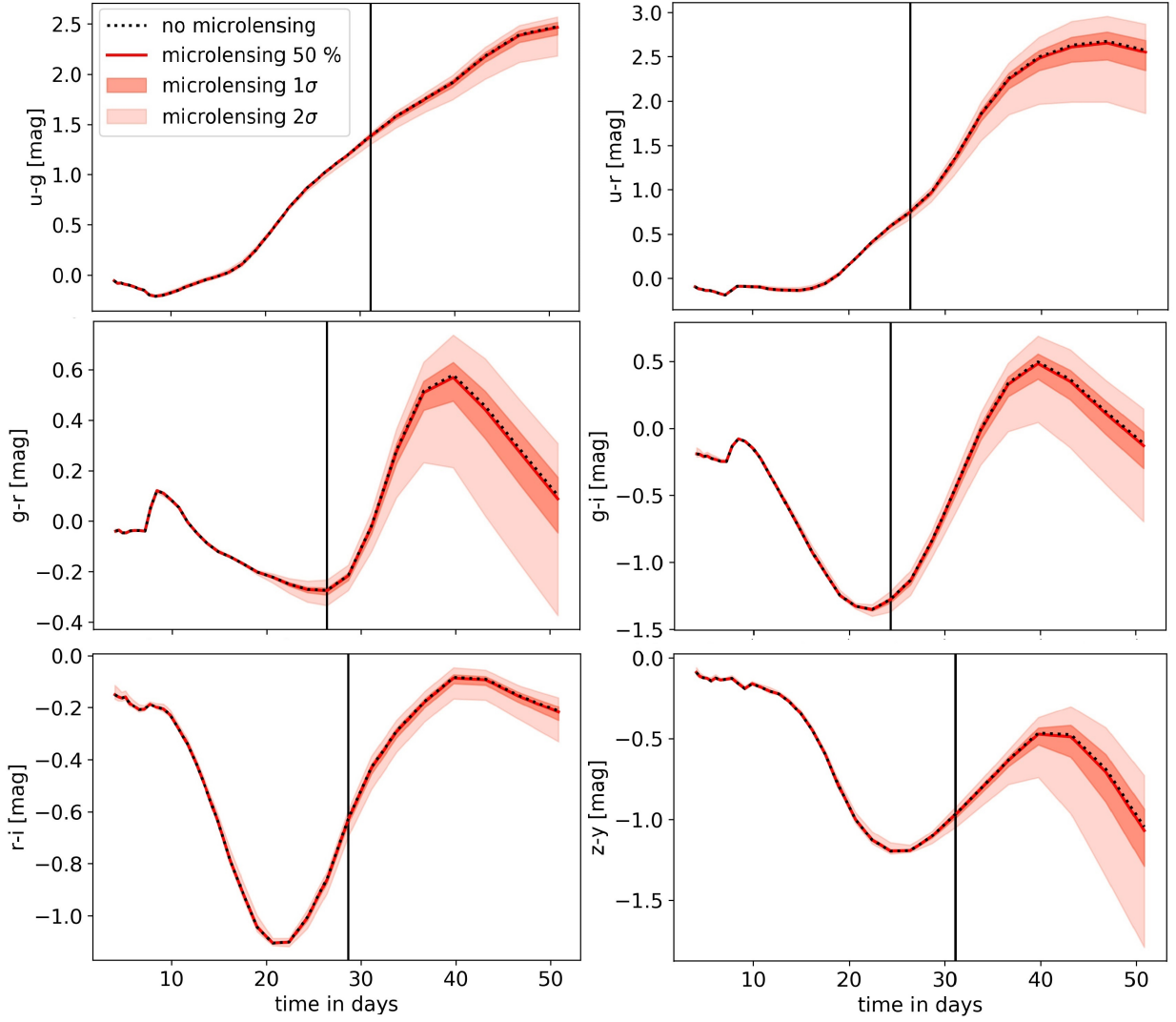


Fig. A.5: These plots compare the non-microlensed color curves (dotted black) to the microlensed ones (with median in solid red, and the  $1\sigma$  and  $2\sigma$  range in different shades), for 10000 random SNe positions in a magnification map. The vertical black line indicates the first time the  $2\sigma$  spread of the microlensed color curves exceeds 0.1 magnitudes. The panels are all rest-frame LSST color curves for a saddle image ( $\kappa = 0.6$ ,  $\gamma = 0.6$  and  $s = 0.6$ , see Figure 1), which show an achromatic phase similar to the one reported by Goldstein et al. (2018b), but we find the achromatic phase only for combinations of the bands  $u$ ,  $g$ ,  $r$  and  $i$  (except  $u-i$ ) and for the color curve  $z-y$  up to  $\sim 25$  to 30 days after explosion.

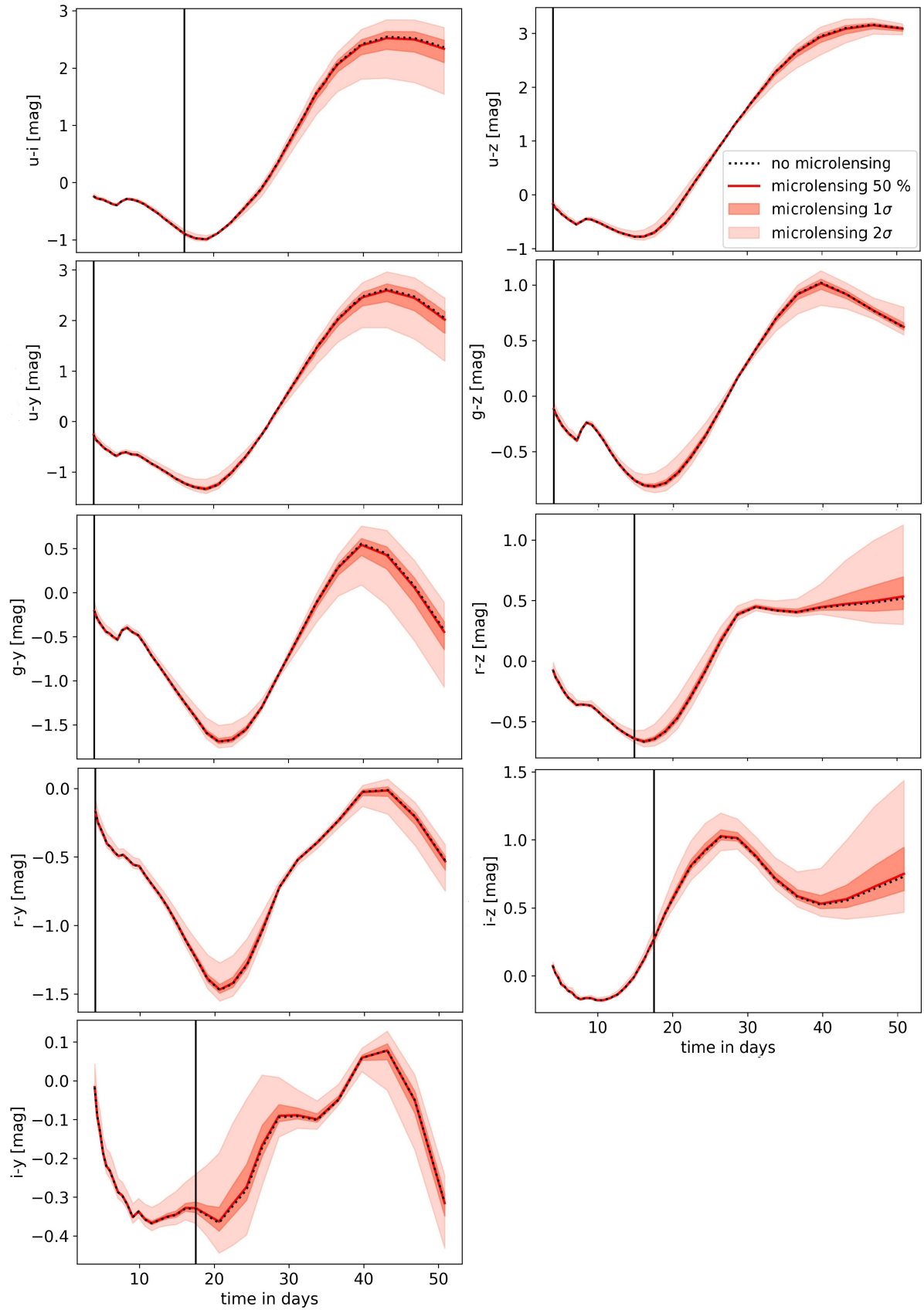


Fig. A.6: Panels are produced similarly to those in Figure A.5, except these colors curves exhibit a shorter or non-existing achromatic phase in comparison to those in Figure A.5.